Supplementary Information

Connectivity dependent thermopower of bridged biphenyl molecules in single-molecule junctions

Iain M. Grace,[1] Gunnar Olsen,[2] Juan Hurtado-Gallego,[3] Laura Rincón-García,[3,4] Gabino Rubio-Bollinger,[3,5] Martin R. Bryce,[2] Nicolás Agraït[3-5] and Colin J. Lambert[1]

1. Department of Physics, Lancaster University, Lancaster, LA1 4YB, UK
2. Department of Chemistry, Durham University, Durham, UK
3. Departamento de Física de la Materia Condensada, Universidad Autónoma de Madrid, E-28049 Madrid, Spain
4. Instituto Madrileño de Estudios Avanzados en Nanociencia IMDEA-Nanociencia, E-28049 Madrid, Spain
5. Condensed Matter Physics Center (IFIMAC) and Instituto Universitario de Ciencia de Materiales "Nicolás Cabrera" (INC), Universidad Autónoma de Madrid, E-28049 Madrid, Spain

Table of Contents

S1. Tight binding model

The following plot show results for the tight binding model of Figure 3a of the main text.
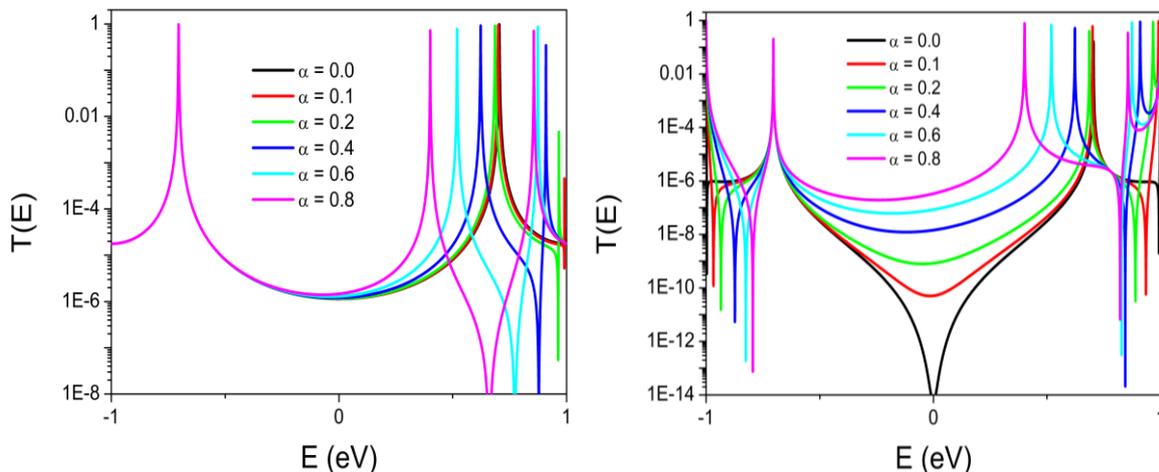
Fig. S1 Transmission coefficients versus electron energy for the tight binding model of Figure 3a. Left panel: *para* connectivity. Right panel: *meta* connectivity (Γ=0.08γ).
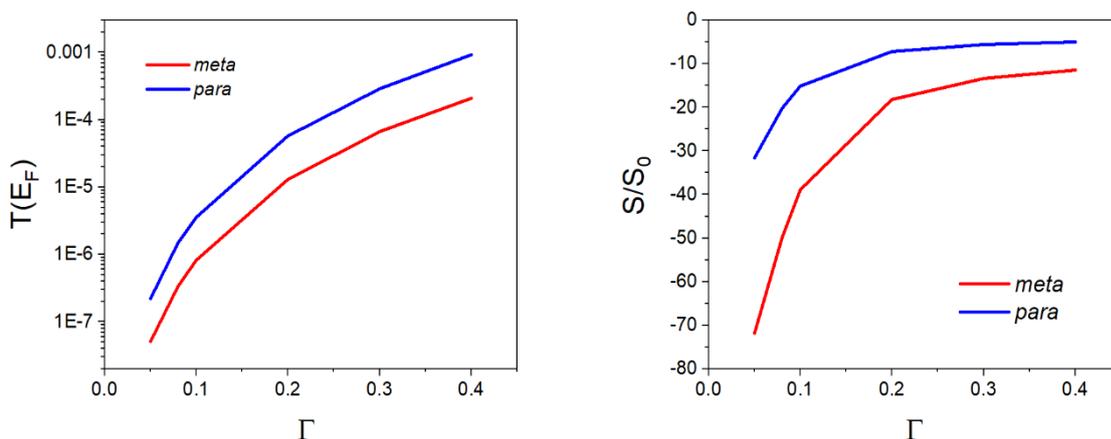
Fig. S2 Left Panel: Plots of $T(E_F)$ versus the coupling strength Γ to the leads. Right Panel: Plots of S/S_0 versus the coupling strength Γ to the leads. (α=0.8)
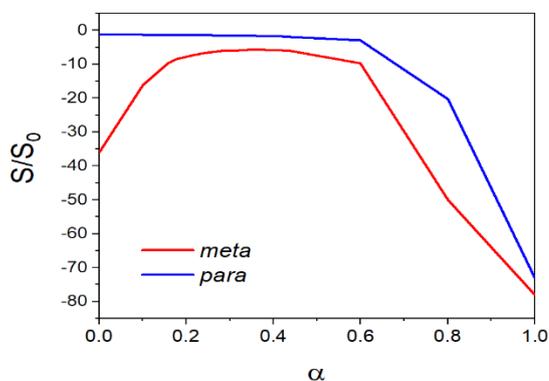
Fig. S3 Room temperature Seebeck coefficient versus $α$ obtained from the transmission plots of Figure S1.

2

S2. Electronic structure calculations

Theoretical method

The optimum geometry of each of the molecules was calculated using the density functional code SIESTA. These used a double-zeta (DZ) basis set defined by a confining cut-off of 0.003 Rydbergs, norm conserving pseudopotentials, an energy cut-off of 150 Rydbergs and the GGA method[1] to describe the exchange correlation functional. All forces on the atoms were relaxed to a force tolerance of 0.01 eV/Å. The molecule was then attached to gold electrodes which we model with pyramid tips attached to 6 layers of (111) gold each containing 25 atoms, and a Hamiltonian describing this extended molecule was extracted using SIESTA[2]. The zero bias transmission coefficient $T(E)$ and the Seebeck coefficient were calculated using the quantum transport code Gollum[3].

HOMO and LUMO Kohn-Sham eigenvalues

X	Para			Meta		
	HOMO (eV)	LUMO (eV)	Eg (eV)	HOMO (eV)	LUMO (eV)	Eg (eV)
CH_2	-4.95	-1.98	2.97	-5.02	-1.63	3.39
S	-4.93	-2.04	2.89	-4.85	-1.65	3.20
CMe_2	-4.93	-1.99	2.94	-5.02	-1.65	3.37
O	-5.08	-2.04	3.04	-5.05	-1.70	3.35
NEt	-4.68	-1.88	2.8	-4.61	-1.50	3.11
C=O	-5.12	-2.84	2.28	-5.10	-2.87	2.23
SO_2	-5.29	-2.36	2.93	-5.24	-2.47	2.77

Table S1. The Kohn Sham eigenvalues of each molecule evaluated in the gas phase.

HOMO and LUMO orbitals
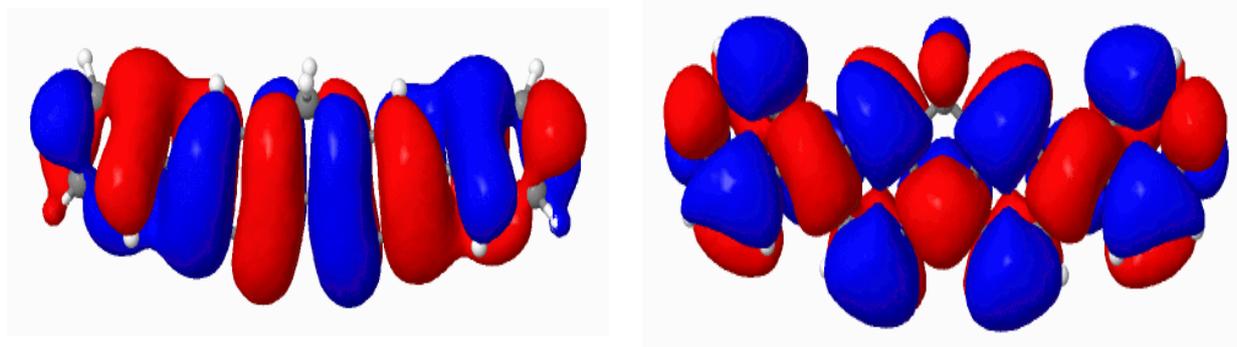

Fig. S4 HOMO (left) and LUMO (right) for **X** = CH$_2$ *para*.
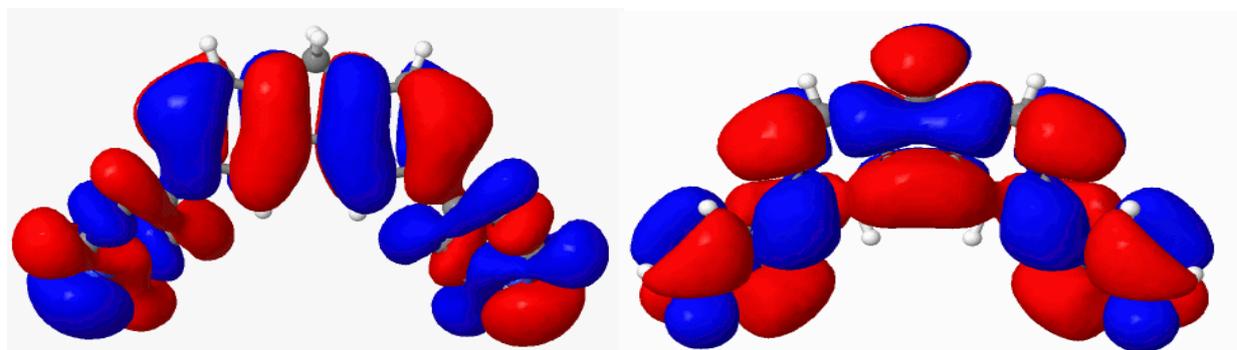
Fig. S5 HOMO (left) and LUMO (right) for **X** = CH$_2$ *meta*.
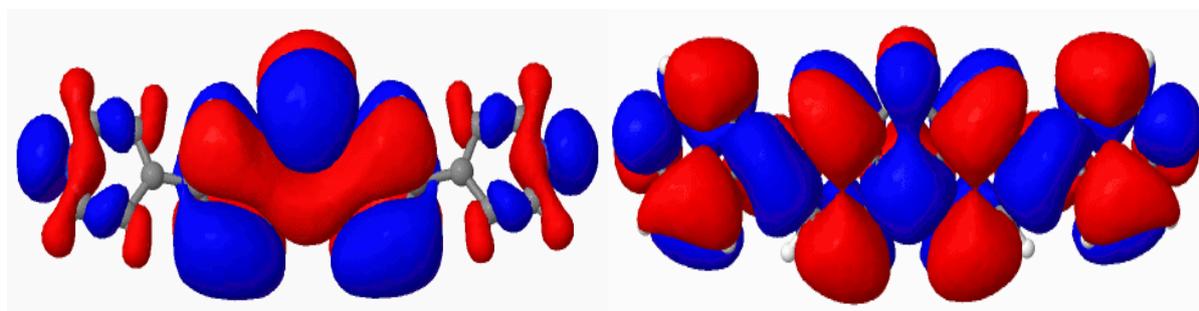

**Fig. S6** HOMO (left) and LUMO (right) for **X** = S *para*
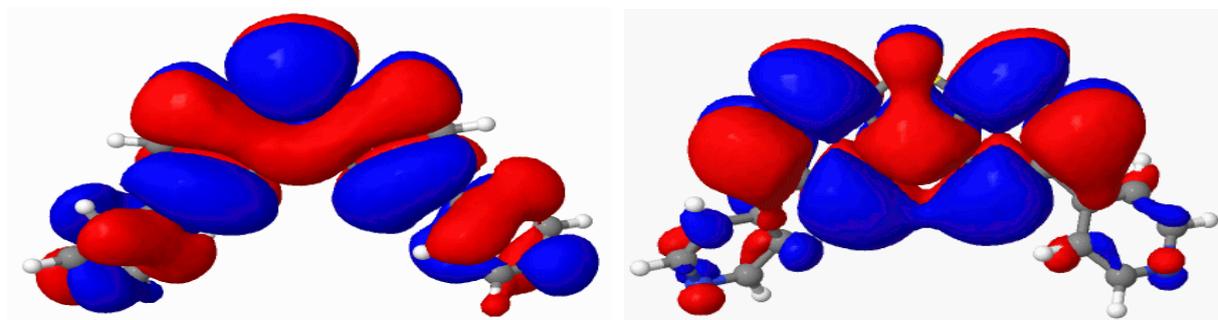
Fig. S7 HOMO (left) and LUMO (right) for **X** = S *meta*
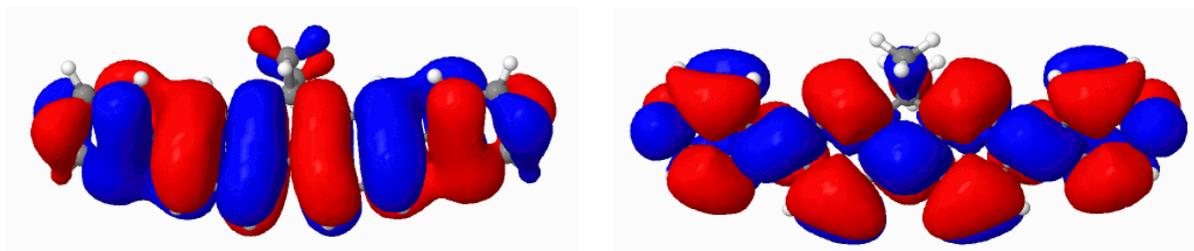
Fig. S8 HOMO (left) and LUMO (right) for **X** = CMe$_2$ *para*.
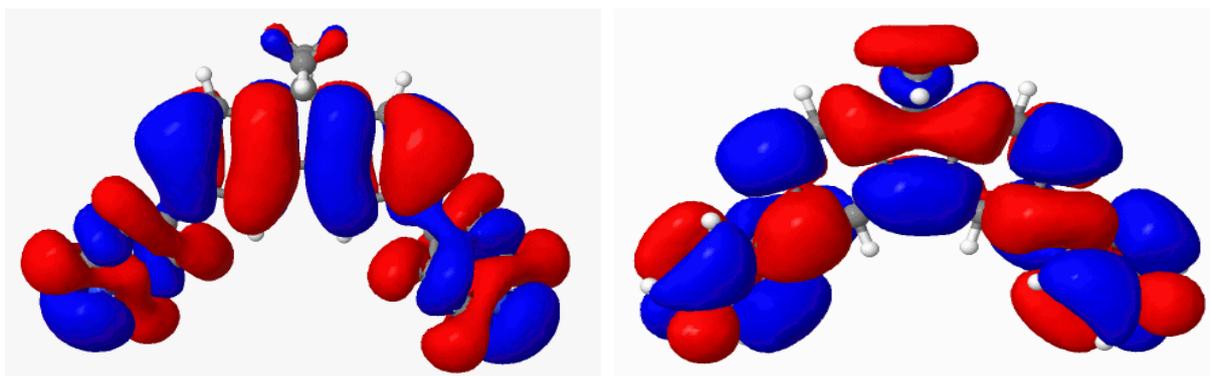
Fig. S9 HOMO (left) and LUMO (right) for **X** = CMe$_2$ *meta*.
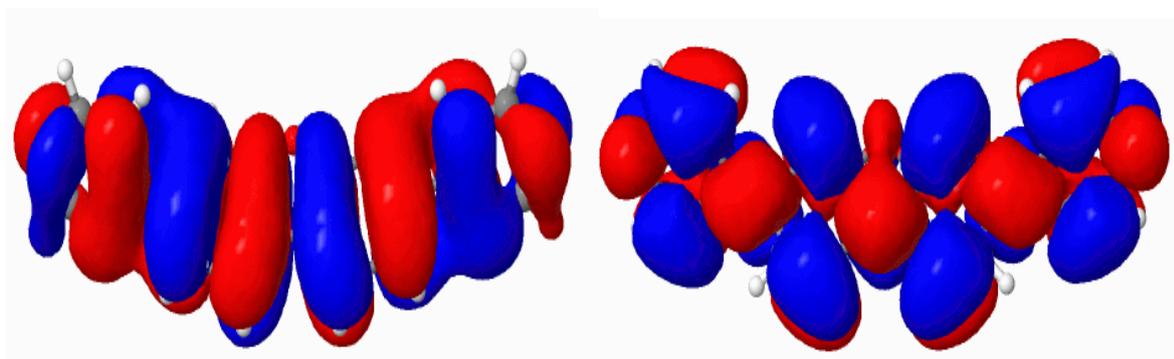

Fig. S11 HOMO (left) and LUMO (right) for **X** = O *para*.
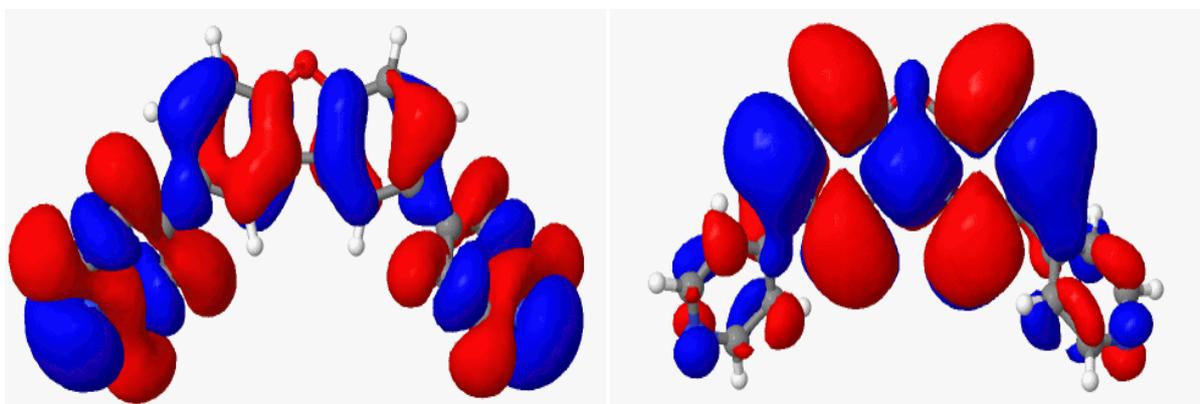

**Fig. S12** HOMO (left) and LUMO (right) for **X** = O *meta*.
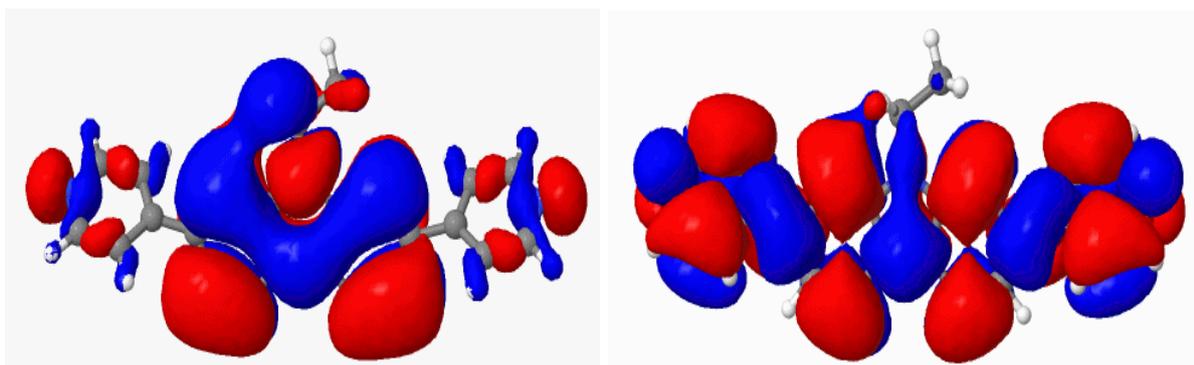
Fig. S13 HOMO (left) and LUMO (right) for **X** = NEt *para*.
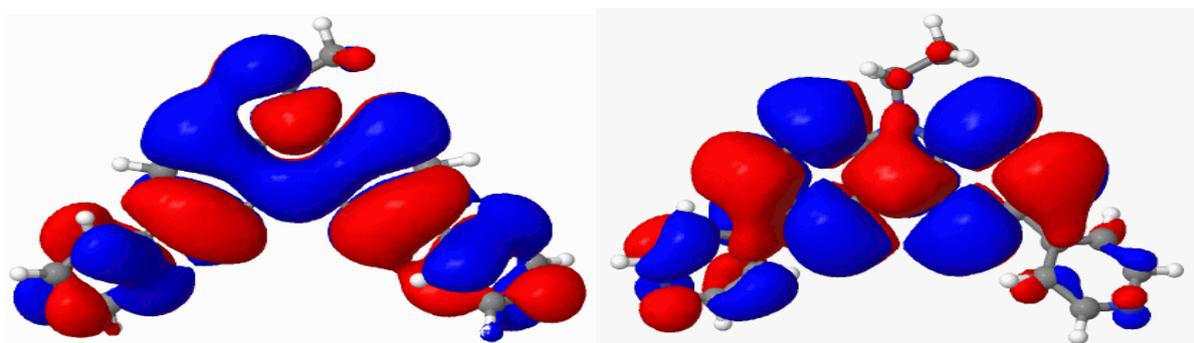

Fig. S14 HOMO (left) and LUMO (right) for **X** = NEt *meta*.
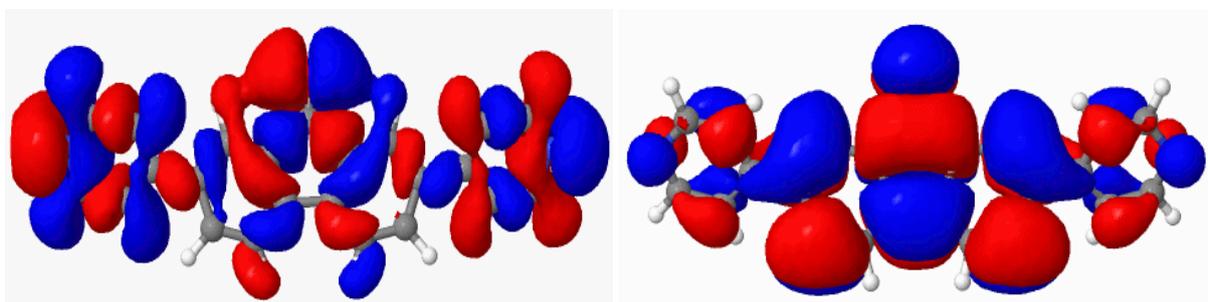

**Fig. S15** HOMO (left) and LUMO (right) for **X** = C=O *para*.
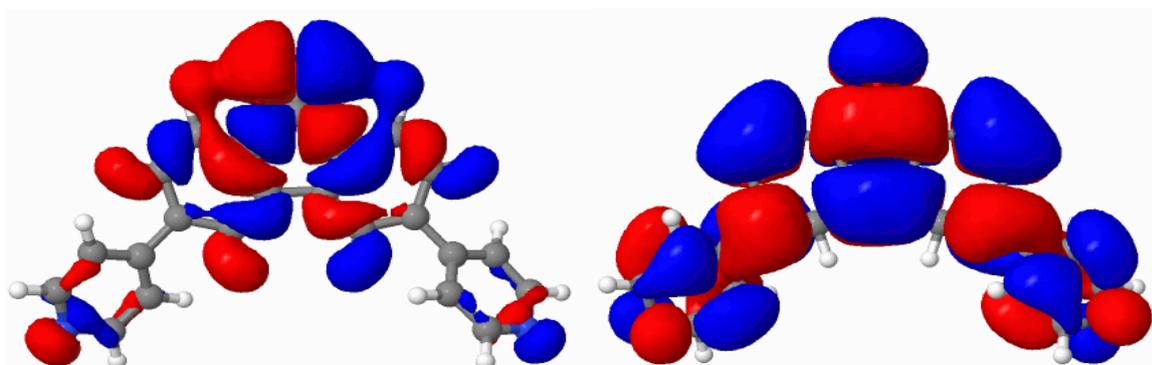


Fig. S16 HOMO (left) and LUMO (right) for **X** = C=O *meta*.
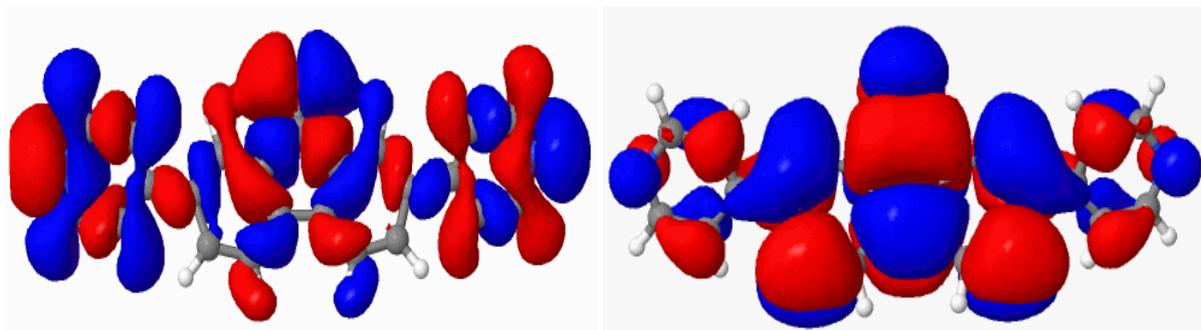
**Fig. S17** HOMO (left) and LUMO (right) for **X** = SO$_2$ *para*
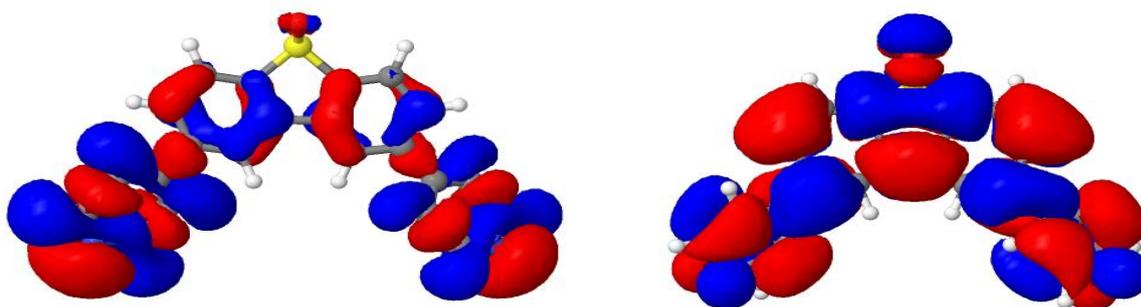
**Fig. S18** HOMO (left) and LUMO (right) for **X** = SO$_2$ *meta*

S3. Quantum transport Calculations

Contact geometry

The series of molecules in Figure 1 consist of a central bridged biphenyl core with pyridine rings attached either in the *meta* or *para* position to form the anchor groups which contact to gold electrodes. To model the expected behaviour in a break junction, the gold electrodes were terminated with a pyramid of atoms, such that the terminal nitrogen atom of each pyridyl ring makes contact to the tip gold atom. The optimum binding distance d was then calculated between the gold tip and the nitrogen atom (Figure S19(a)) by evaluating the binding energy as a function of d. Here the system was treated as a two-component object, where the gold electrode is A and the molecule is B. Due to basis set superposition errors (BSSE), when using a localized basis set we used a counterpoise method to evaluate the binding energy E_{bind}. This is given by the following equation:

$$E_{bind} = E_{AB}^{AB} - \left(E_A^{AB} + E_B^{AB} \right)$$

Where E_{AB}^{AB} is the ground state energy of the gold electrode (A) and molecule (B), E_A^{AB} is the energy of the gold (A) in the basis of the dimer AB and E_B^{AB} is the energy of the molecule in the basis of the dimer AB. Figure S19 (b) shows that the optimum binding distance d is 2.4 Å and the magnitude of the binding energy is 0.6 eV. Note, the parameters are consistent with the method described above in theoretical method.

7
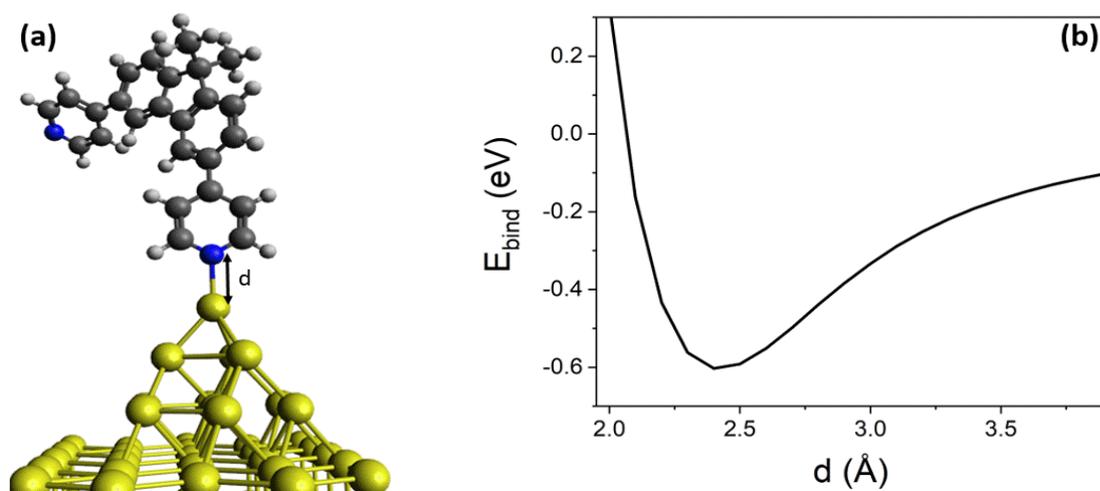
Fig S19. (a) Binding geometry as a function of the gold-nitrogen distance d. (b) Binding energy E_{bind} as a function of d.

Basis set dependence

In the case of pyridine anchor groups, the position of the Fermi energy relative to the molecular resonances depends on the nature of the basis set. SIESTA uses a basis set formed from local atomic orbitals, and the extent of the orbitals can be controlled by the energy cut-off (i.e. the value beyond which the orbital is zero). For example, a value of 0.03 Rydbergs gives a short cut-off and decreasing the energy cut-off value increases the cut-off radius for the orbitals of each atom. As an example, we take the molecules with **X** = CMe$_2$, attach the electrodes in the optimum binding geometry (d=2.4 Å) and calculate the zero bias transmission coefficient $T(E)$ for the varying basis set. Figure S20 for the *para* connection and *meta*, both show that for short value cut-offs (0.03 Ry) the LUMO resonance lies close to 0 eV, and as the cut-off value is decreased the resonance shifts further away from E_F. Figure S21 show the effect of this on the calculated conductance and Seebeck coefficient. The short basis set gives a large conductance and Seebeck coefficient, we therefore chose to use a basis set defined by a cut-off value of 0.003 Ry, which positions the Fermi energy towards the middle of the HOMO-LUMO gap. The measured values of the Seebeck coefficient for these molecules suggest that the Fermi energy is located well away from the molecular resonances.
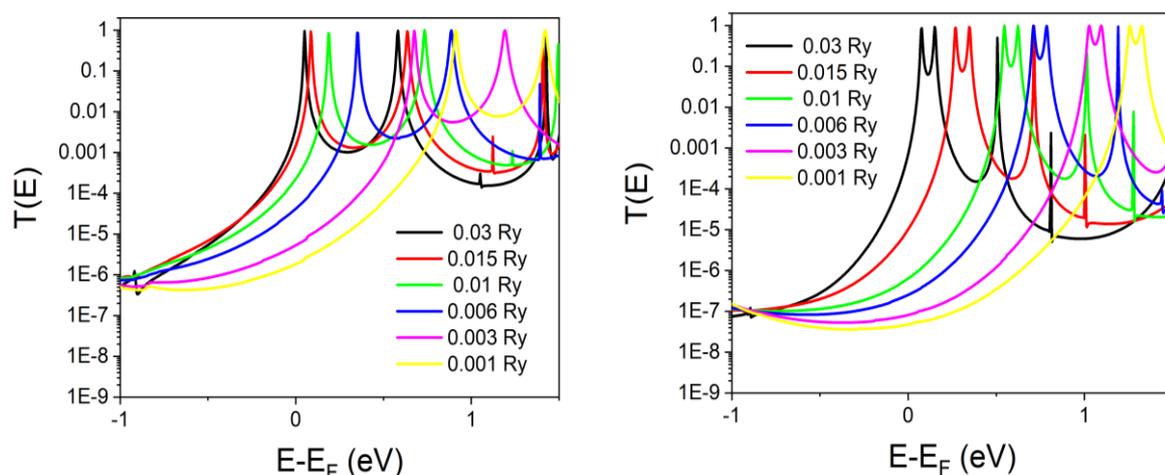

Fig. S20 Transmission coefficient $T(E)$ for different basis set energy cut-off values **X** = CMe$_2$ *para* (left panel), **X** = CMe$_2$ *meta* (right panel).

8
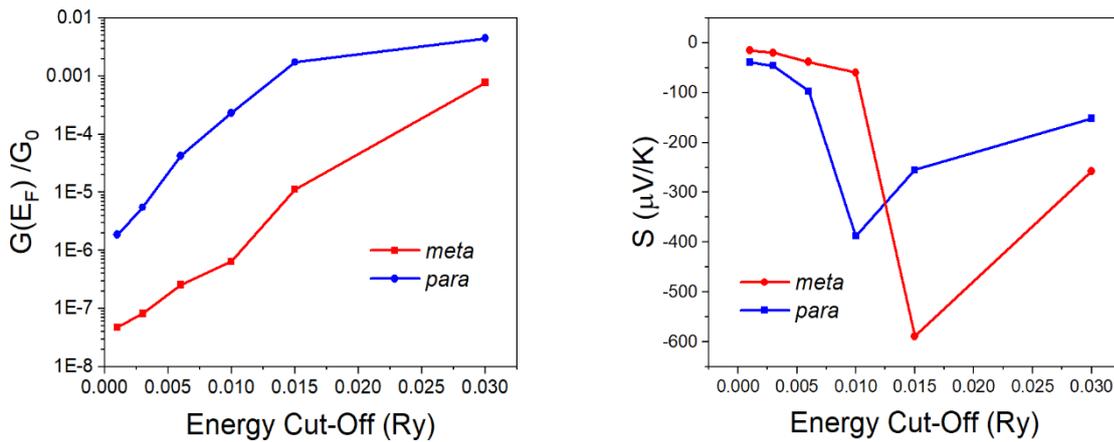
Fig. S21 Conductance (left panel) and Seebeck coefficient (right panel) evaluated at E_F as a function of the basis set cut-off.

Transmission coefficients for *meta* and *para* series

Figure S22 shows $T(E)$ for each value of the bridging atom **X** for the *meta* (Figure 7a) and *para* (Figure 7b) connections using the parameters described in the theoretical method. We evaluate the *para* series for all values of **X**, although only three have been experimentally measured. For both series we do not see any destructive interference features in the HOMO-LUMO gap. The results show a strong dependence on the bridging atom, with the LUMO resonance shifting relative to the DFT-predicted E_F. For **X** = C=O and **X** = SO$_2$ the LUMO resonance sits closer to E_F which is related to the more conjugated nature of these two bridges[4].
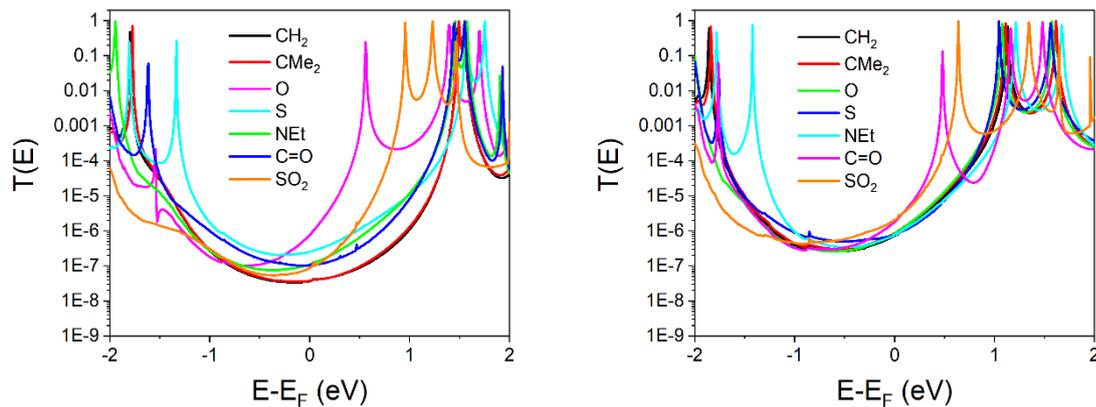

Fig. S22 Transmission coefficient T(E) as a function of electron energy E for fluorene series. *Meta* (left panel) connected geometry as shown in figure 7a (*d*=2.4 Å). *Para* (right panel) connected geometry figure 7b (*d*=2.4 Å).

We then compare $T(E)$ and S for each bridging group **X** for the *meta* and *para* connections for a binding distance of d = 2.4 Å. The results shown in Figures S23-S29 show that there is a clear general trend for the *para* connection to give a higher value of S. This is due to the fact that the HOMO-LUMO gap is smaller and has a lower-energy LUMO (see Table 1 main paper) meaning that the resonance sits closer to the Fermi energy for the *para* case. Whereas the tight binding model (Figure 2 main paper), which only takes into account the core, predicts the *meta* connection will have a higher S, because the HOMO-LUMO gap does not change.
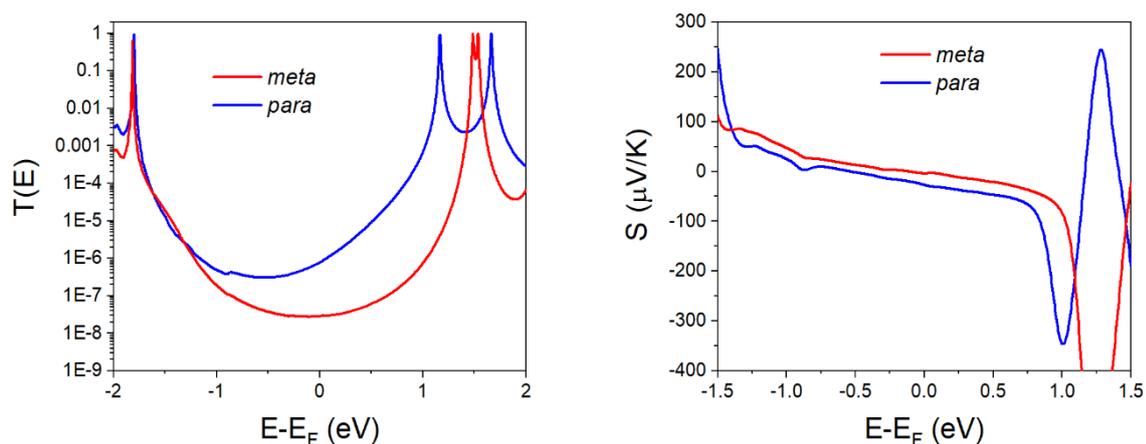
Fig. S23 Comparison between *para* and *meta* connectivity for **X** = CH_2. Transmission coefficient (left panel) Seebeck coefficient (right panel).
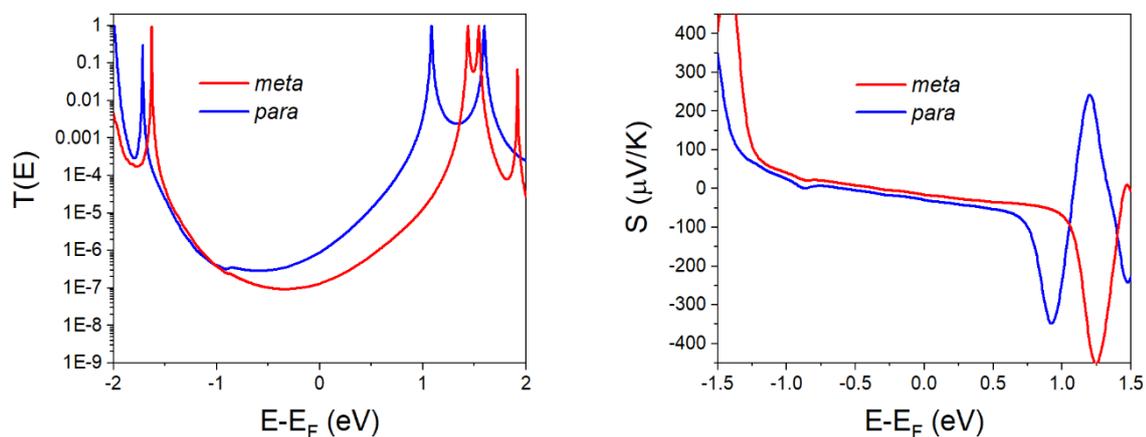
Fig. S24 Comparison between *para* and *meta* connectivity for **X** = S. Transmission coefficient (left panel) Seebeck coefficient (right panel).
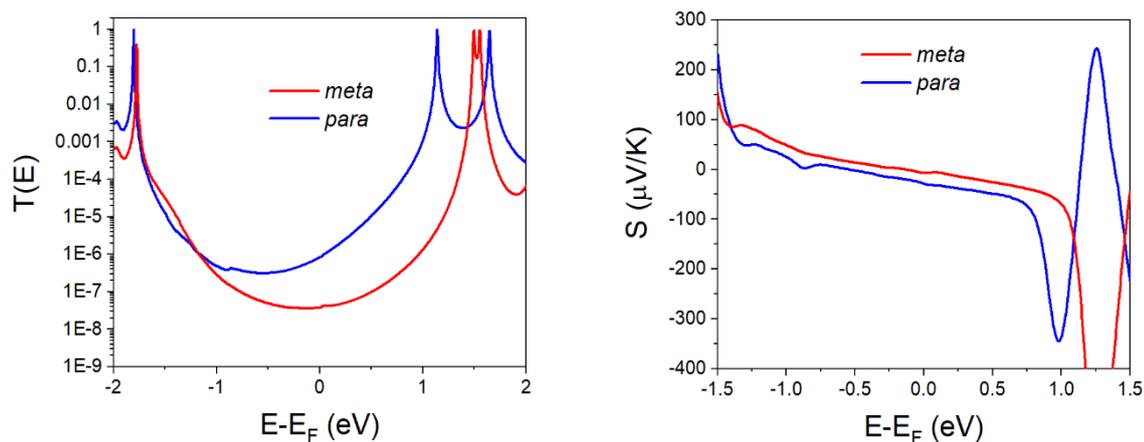
Fig. S25 Comparison between *para* and *meta* connectivity for **X** = CMe$_2$. Transmission coefficient (left panel) Seebeck coefficient (right panel).
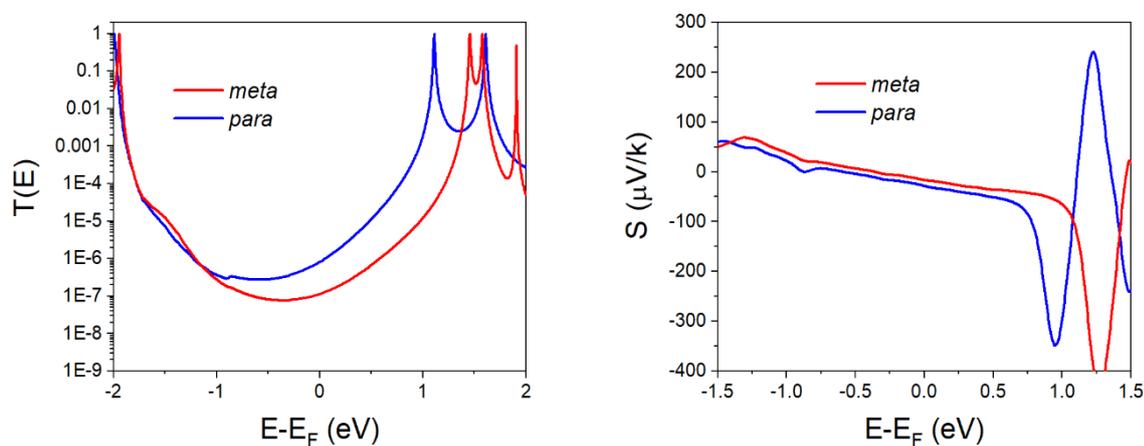
Fig. S26 Comparison between *para* and *meta* connectivity for **X** = O. Transmission coefficient (left panel) Seebeck coefficient (right panel).
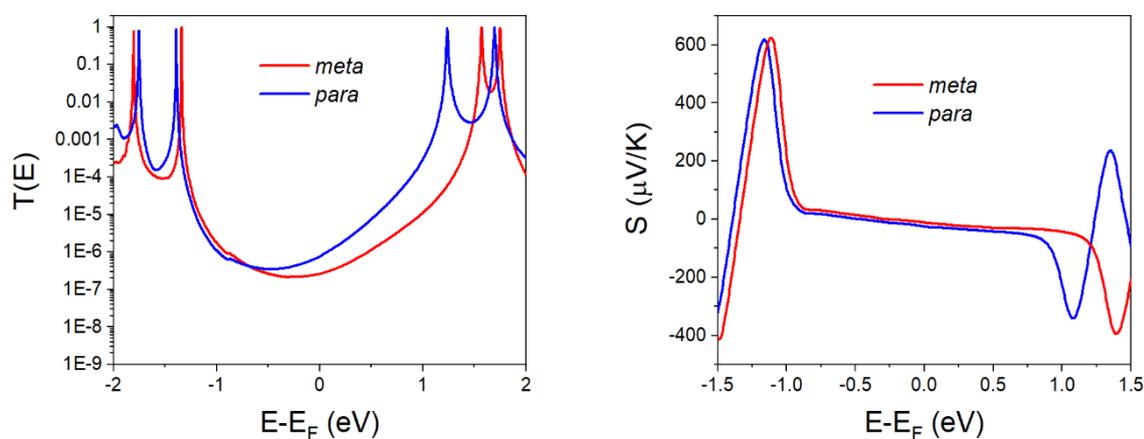
Fig. S27 Comparison between *para* and *meta* connectivity for **X** = NEt. Transmission coefficient (left panel) Seebeck coefficient (right panel).
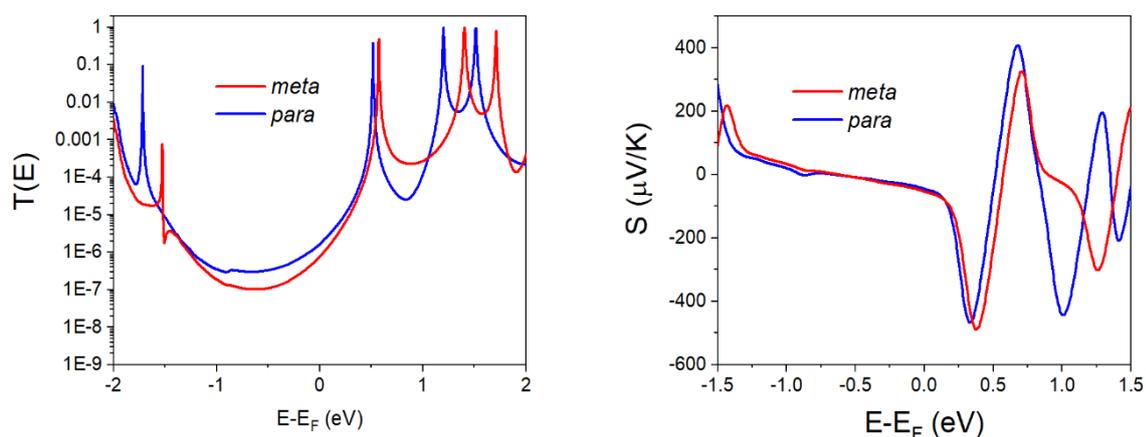
Fig. S28 Comparison between *para* and *meta* connectivity for **X** = C=O.Transmission coefficient (left panel) Seebeck coefficient (right panel).
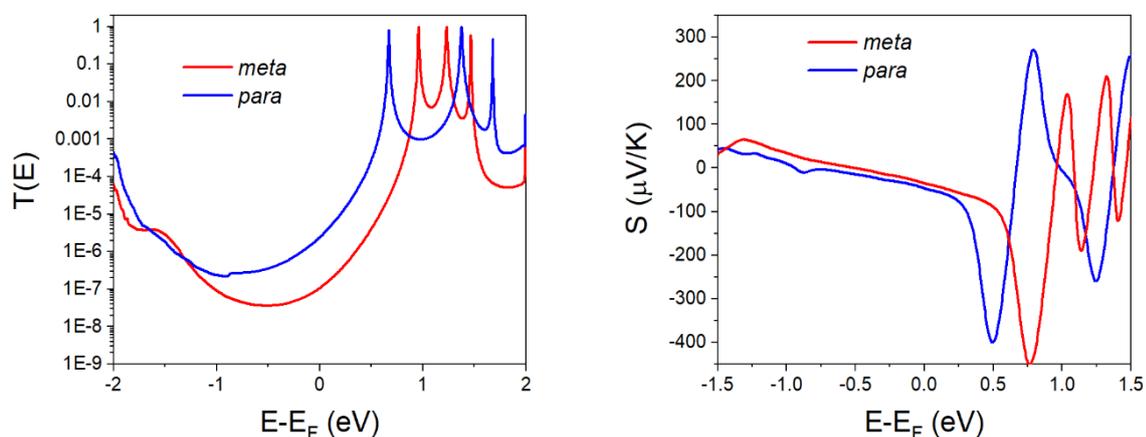
Fig. S29 Comparison between *para* and *meta* connectivity for **X** = SO$_2$. Transmission coefficient (left panel) Seebeck coefficient (right panel).

## Molecule - gold contact strength

In the preceding calculations, it was assumed that the optimum pyridine binding geometry is the same for both the *para* and *meta* molecules. Identical contact geometries are unlikely to form in a break junction measurement, due to the differences in molecular shapes (the *para* is more linear). The unknown nature of both the shape of the gold electrodes and the contact separation between electrodes means a geometry relaxation within the junction is beyond the scope of these calculations due to the number of different parameters that could change. As an example, we now change one parameter, namely the coupling strength between molecule and electrode, by varying the distance d (Figure 7 main paper) and keeping the contact angle constant. Figure S30 shows the transmission coefficient $T(E)$ for **X** = CH$_2$ for varying contact distances, for both *para* and *meta* isomers. There is a clear shifting of the transmission resonances, so that for weaker coupling the LUMO resonance sits further away from E_F, this shifting can be attributed to the change in charge on the molecule. Figure S31 shows how the conductance and Seebeck coefficient vary with d. In general, the conductance is higher for the *para* connection than the *meta*, although the difference decreases as the coupling

12

strength becomes weaker. The Seebeck coefficient shows that at identical contact strengths, the para gives a higher value than the meta. Since the measured Seebeck coefficient is higher for the meta connectivity, this suggests that the coupling to the electrodes is stronger for *meta* connectivity than for *para*. The trends for the conductance are similar for all bridging groups **X** as shown in the Figures S32-S37.
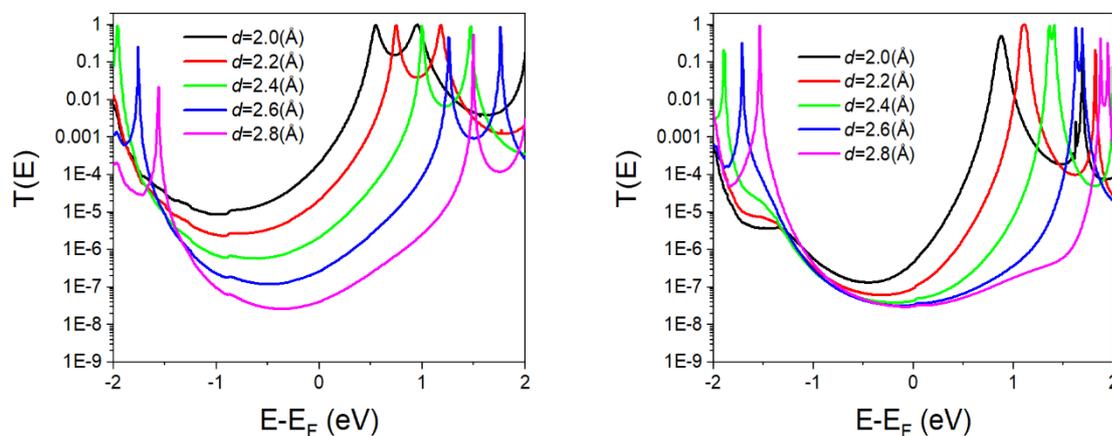

Fig. S30 Transmission coefficient T(E) against electron energy of **X** = CH_2 for varying contact separations d (Figure 7a and b) in the *para* connectivity (left panel) and *meta* connectivity (right panel).
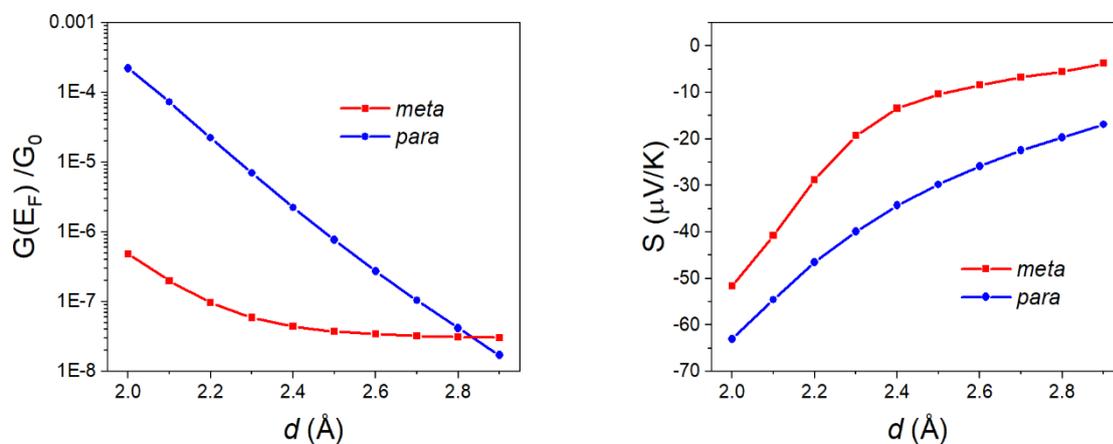
Fig. S31. Molecule **X** = CH_2 (Left panel) Conductance vs contact distance d. (Right panel) Seebeck coefficient versus contact distance d.
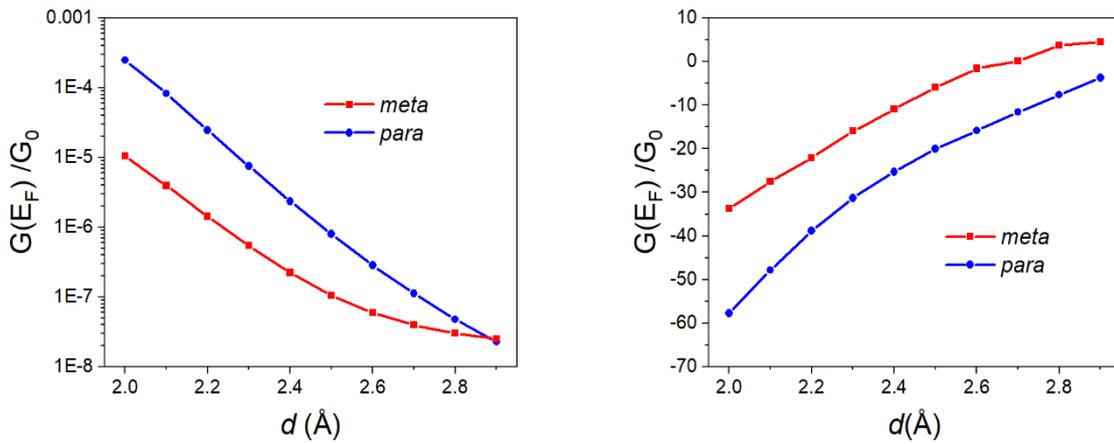
Fig. S32 Molecule **X** = S (Left panel) Conductance vs contact distance d. (Right panel) Seebeck coefficient versus contact distance d.
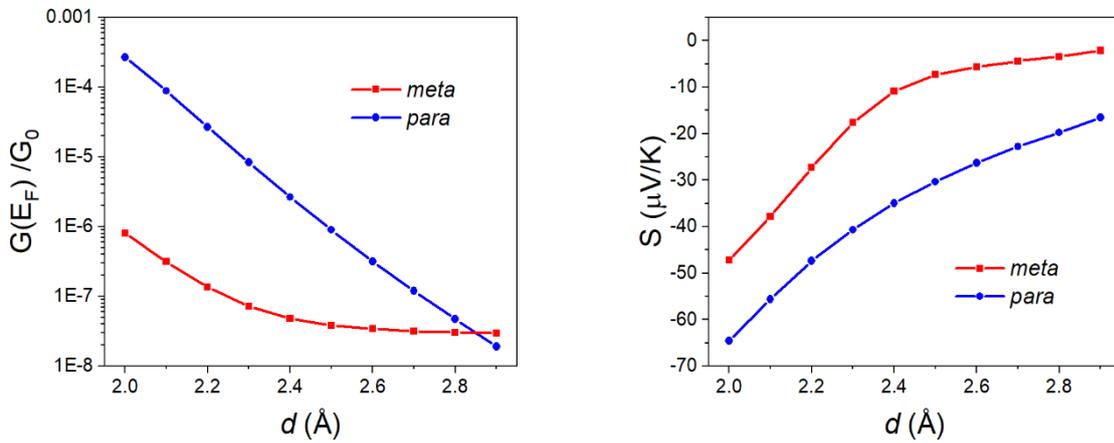
Fig. S33 Molecule **X** = CMe_2 (Left panel) Conductance vs contact distance d. (Right panel) Seebeck coefficient versus contact distance d.
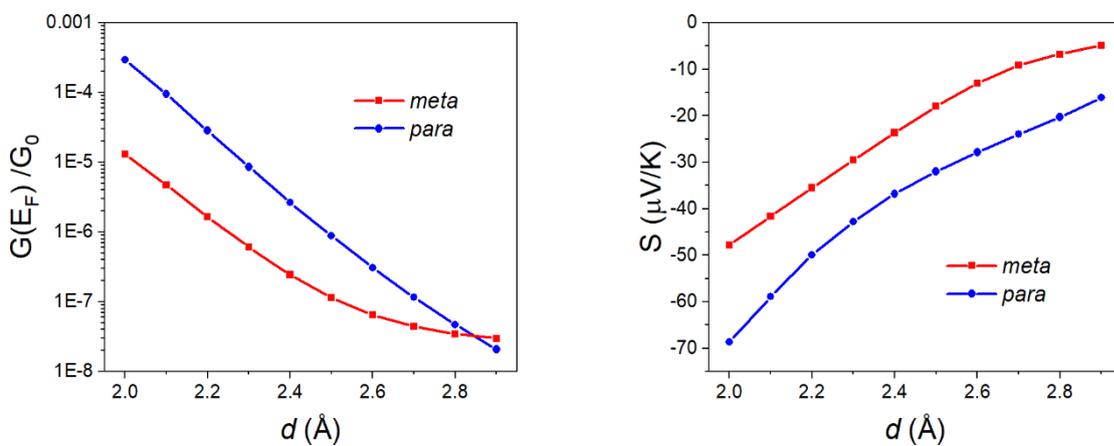
Fig. S34 Molecule **X** = O (Left panel) Conductance vs contact distance d. (Right panel) Seebeck coefficient versus contact distance d.
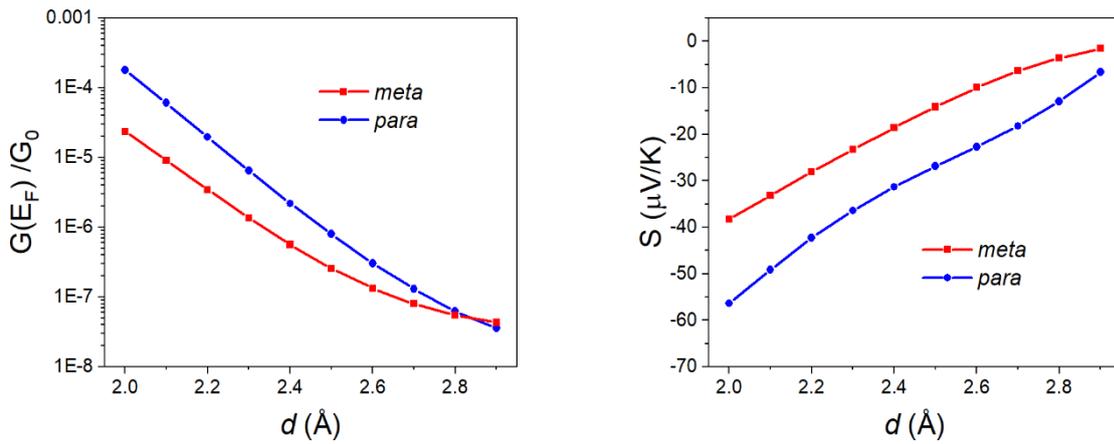
Fig. S35 Molecule **X** = NEt (Left panel) Conductance vs contact distance d. (Right panel) Seebeck coefficient versus contact distance d.
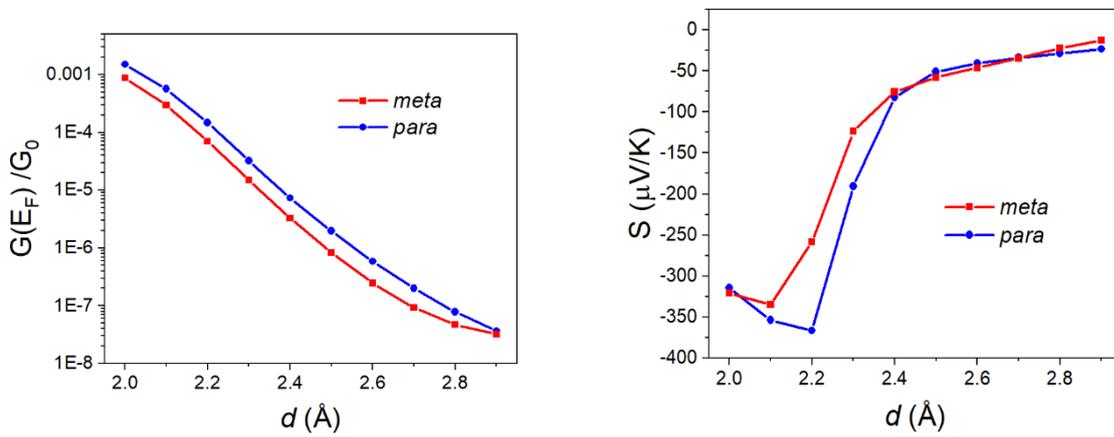

Fig. S36 Molecule **X** = C=O (Left panel) Conductance vs contact distance d. (Right panel) Seebeck coefficient versus contact distance d.
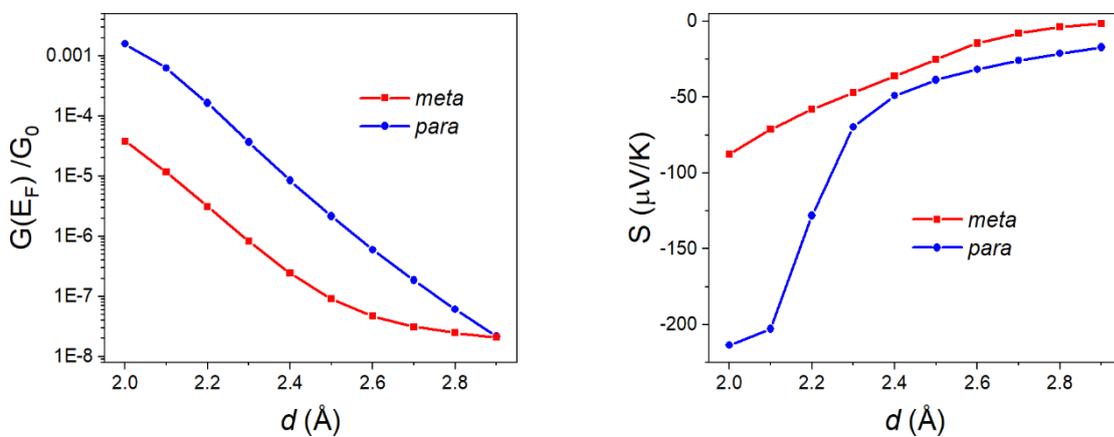

Fig. S37 Molecule **X** = SO_2 (Left panel) Conductance vs contact distance d. (Right panel) Seebeck coefficient versus contact distance d.

Linear contact geometry

To compare with the contact geometry of Figure 7a and b used so far, we now consider a second contact geometry (which we name a linear contact geometry) as shown in Figure S38. In this case the electrodes are aligned, and the axis of the molecule between the terminating nitrogen atoms is aligned with the transport axis, i.e. the normal of the gold electrode surfaces (Figure S38). We then define a contact angle θ (figure S54) to determine this. For the linear contact geometry $\theta=0°$. In this case the *meta* connection forms a very different binding geometry than the *para* connection, with increased interaction between the gold tip and the π system of the pyridine ring. The above transport calculations are then repeated for this second contact geometry. In figures S39-45 the Au-N contact distance d is 2.4Å.
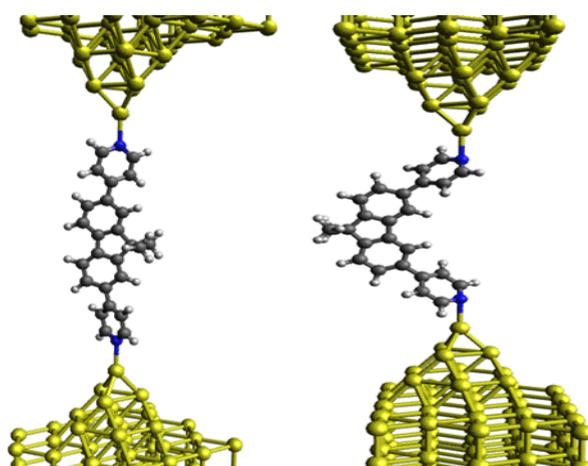

Fig. S38 Linear contact geometry for the *para* connection (left) and *meta* connection (right) for **X** = CMe_2.

Linear contact geometry transmission coefficients for meta and para series
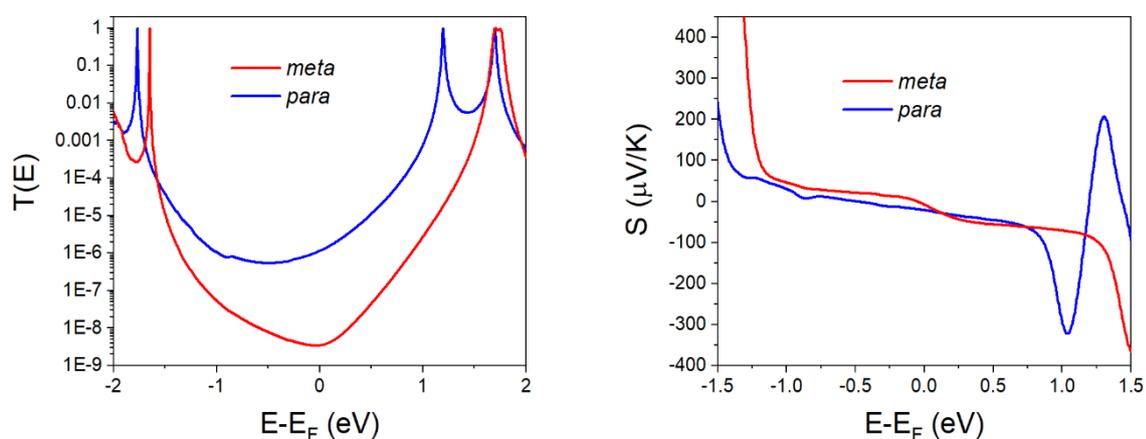
Fig. S39 Linear contact geometry comparison between *para* and *meta* connectivity for **X** = CH_2. (left panel) Transmission coefficient (right panel) Seebeck coefficient.
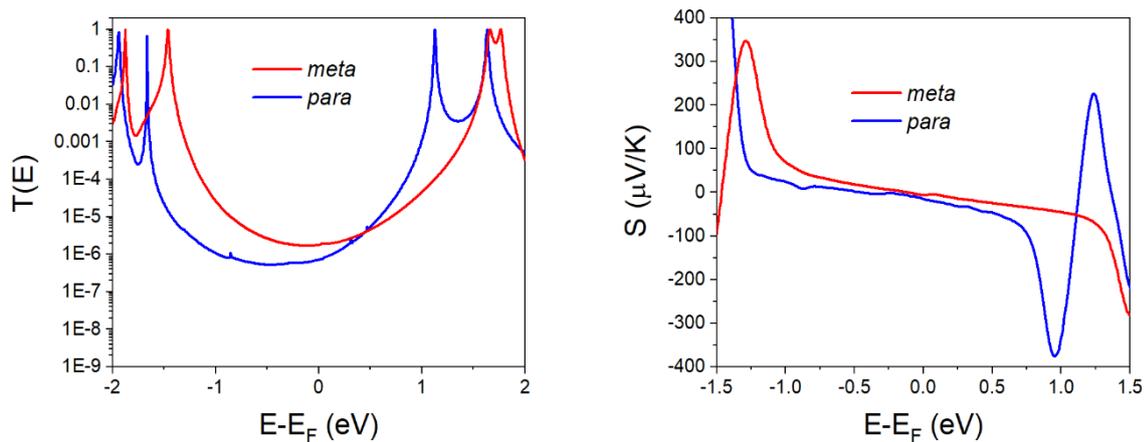
Fig. S40 Linear contact geometry comparison between *para* and *meta* connectivity for **X** = S. (left panel) Transmission coefficient (right panel) Seebeck coefficient.
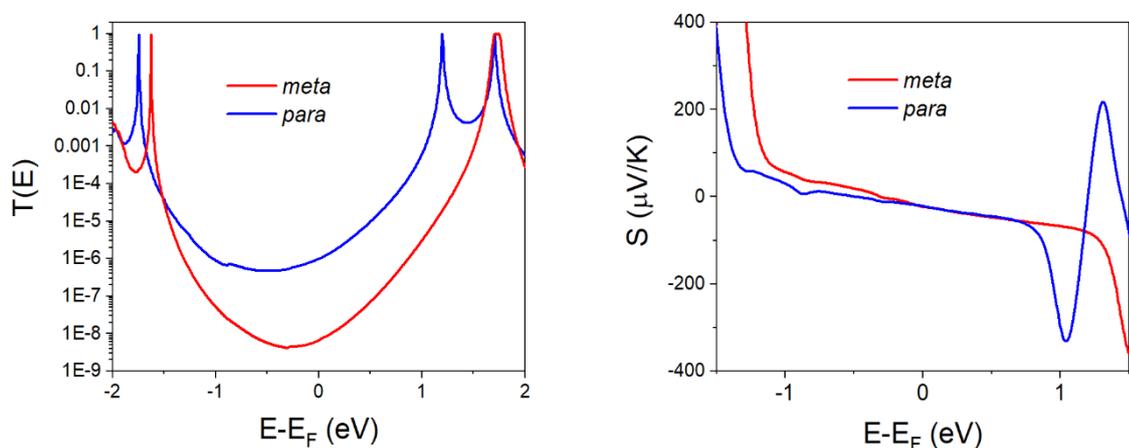
Fig. S41 Linear contact geometry comparison between *para* and *meta* connectivity for **X** = CMe₂. (left panel) Transmission coefficient (right panel) Seebeck coefficient.
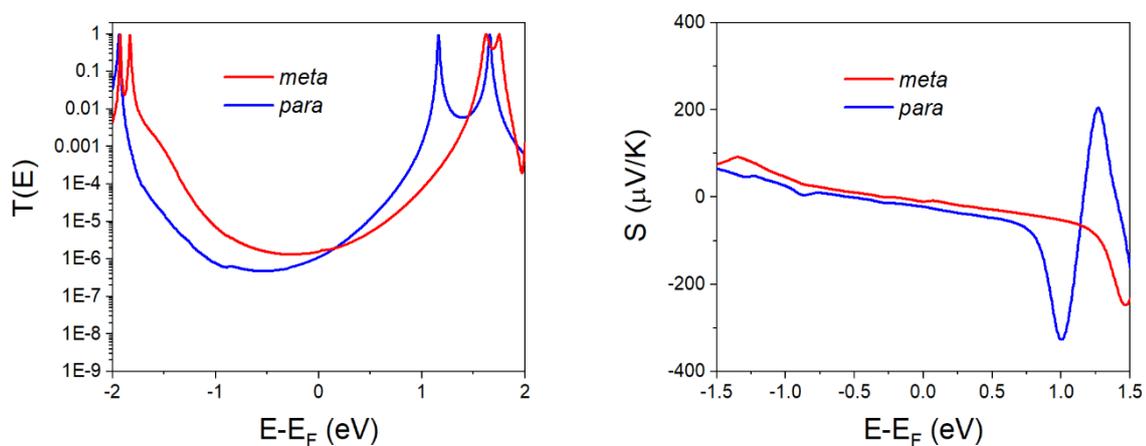
Fig. S42 Linear contact geometry comparison between *para* and *meta* connectivity for **X** = O. (left panel) Transmission coefficient (right panel) Seebeck coefficient.
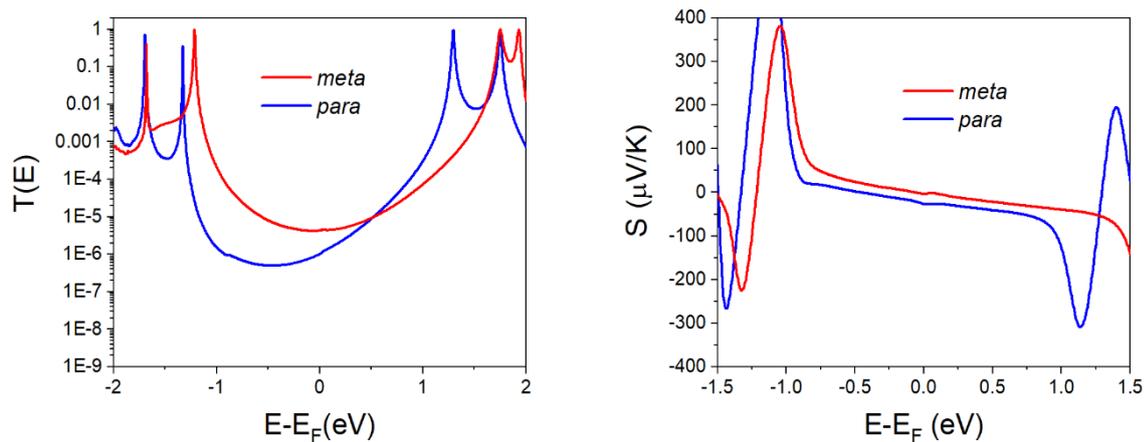
Fig. S43 Linear contact geometry comparison between *para* and *meta* connectivity for **X** = NEt. (left panel) Transmission coefficient (right panel) Seebeck coefficient.
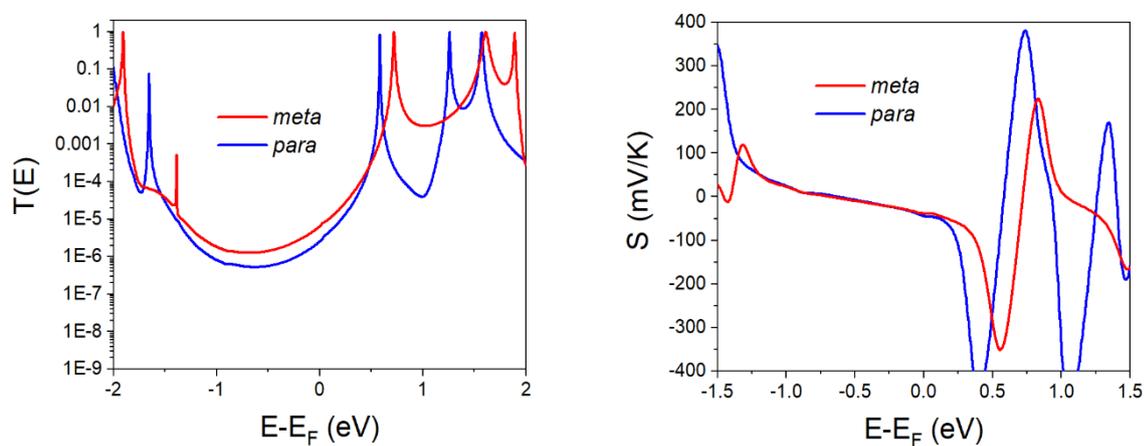
Fig. S44 Linear contact geometry comparison between *para* and *meta* connectivity for **X** = C=O. (left panel) Transmission coefficient (right panel) Seebeck coefficient.
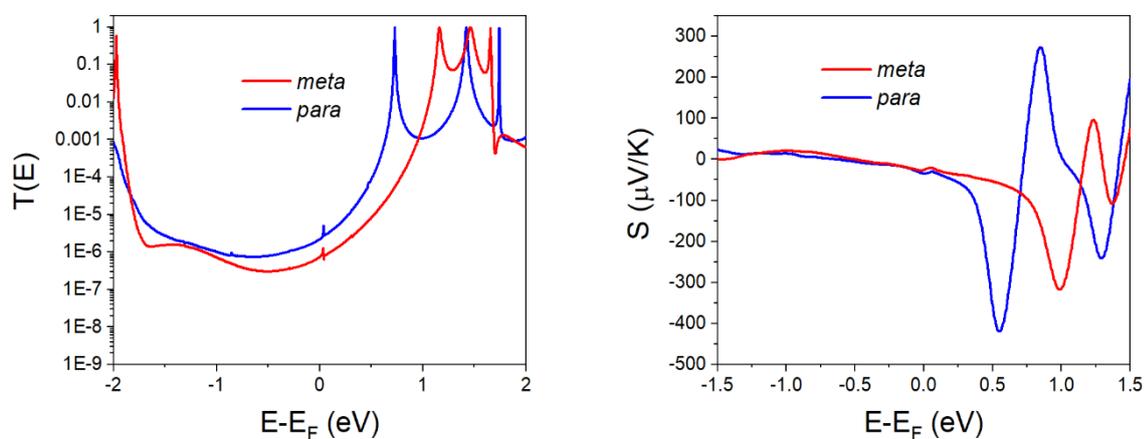

Fig. S45 Linear contact geometry comparison between *para* and *meta* connectivity for **X** = SO$_2$. (left panel) Transmission coefficient (right panel) Seebeck coefficient.

Linear contact geometry - gold contact strength
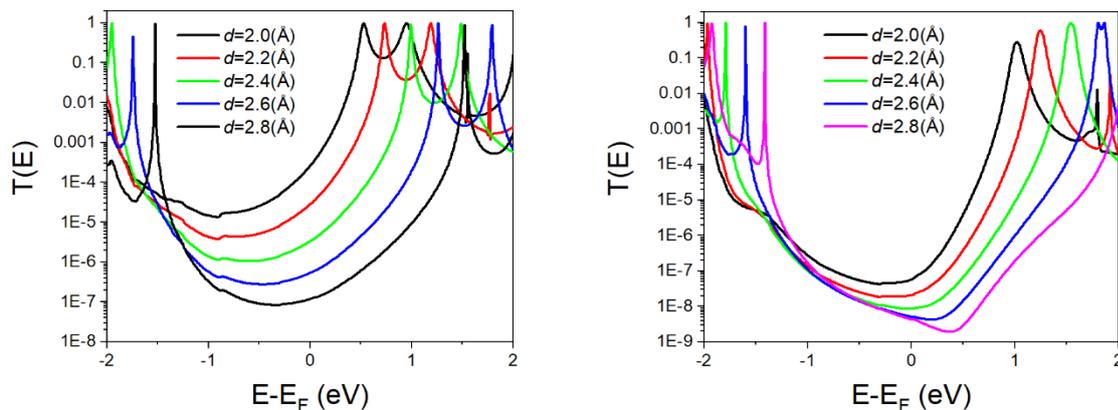
Fig. S46 Transmission coefficient $T(E)$ for varying contact distance d in the linear geometry. (Left) **X** = CH$_2$ *para*. (Right) **X** = CH$_2$ *meta*.
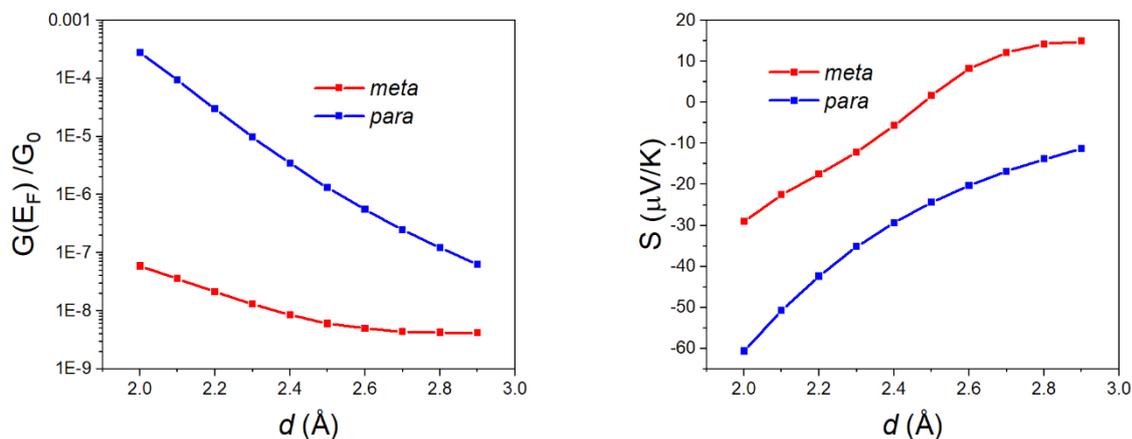
Fig. S47 X = CH$_2$ in a linear geometry. (Left) Conductance vs contact distance d. (Right) Seebeck coefficient against contact distance d.
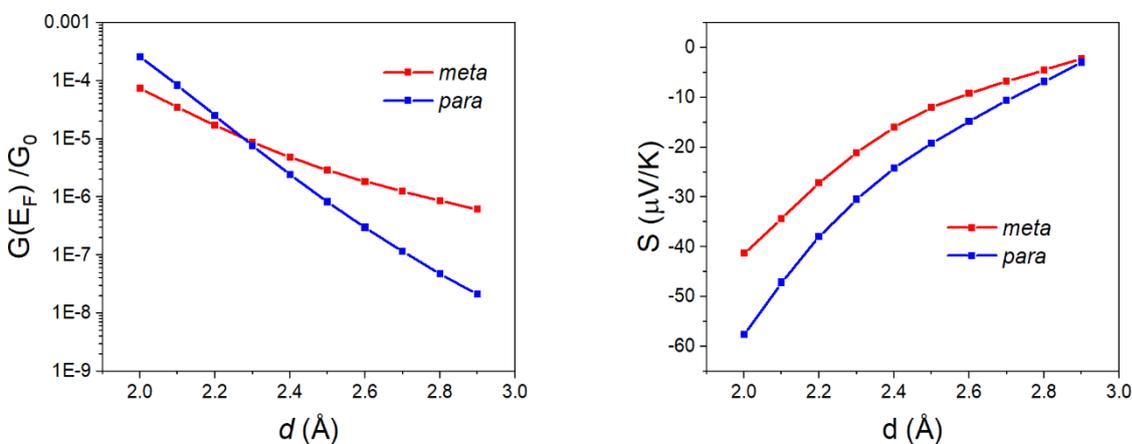
Figure S48 X = S in a linear geometry. (Left) Conductance vs contact distance d. (Right) Seebeck coefficient against contact distance d.
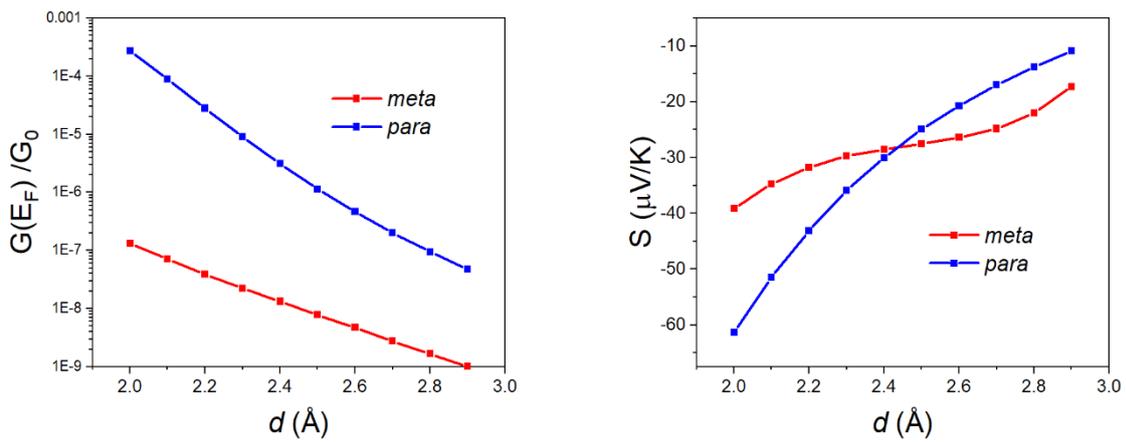
Fig. S49 X = CMe$_2$ in a linear geometry. (Left) Conductance vs contact distance d. (Right) Seebeck coefficient against contact distance d.
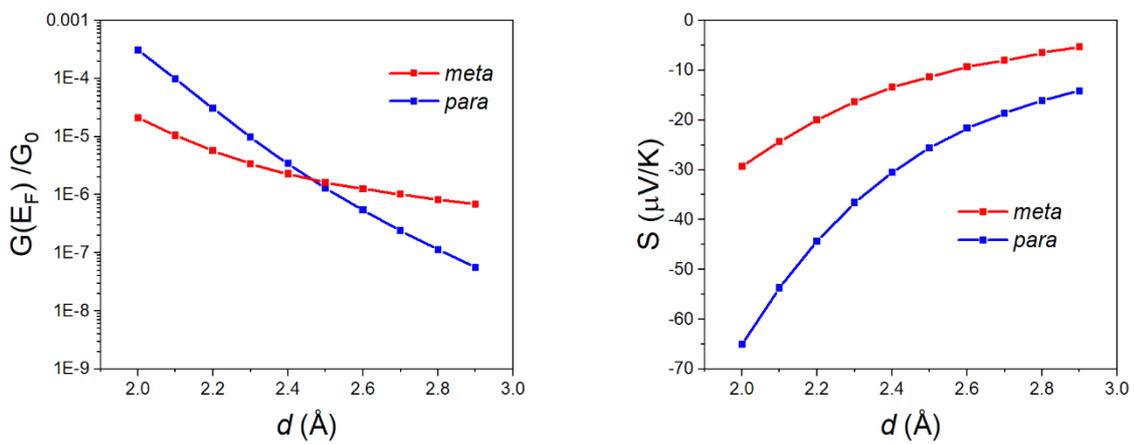
Fig. S50 X = O in a linear geometry. (Left) Conductance vs contact distance d. (Right) Seebeck coefficient against contact distance d.
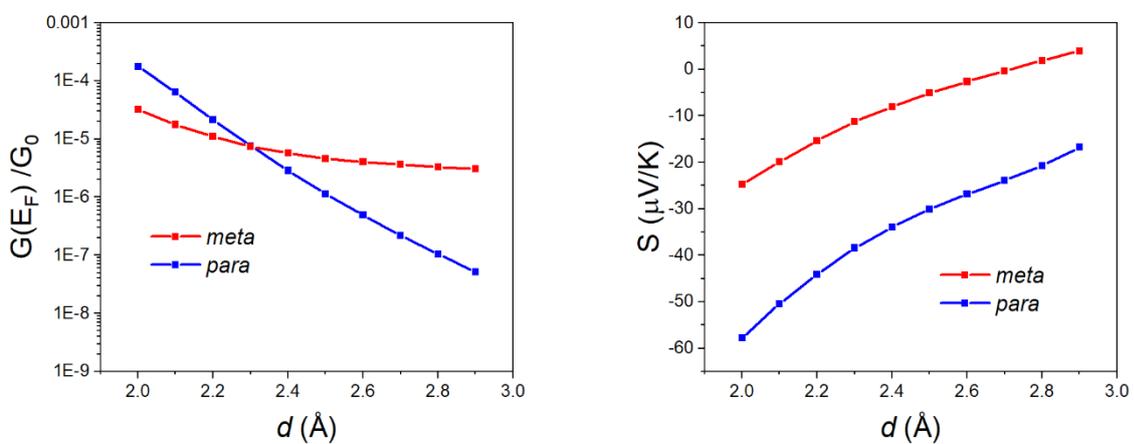
Fig. S51 X = NEt in a linear geometry. (Left) Conductance vs contact distance d. (Right) Seebeck coefficient against contact distance d.
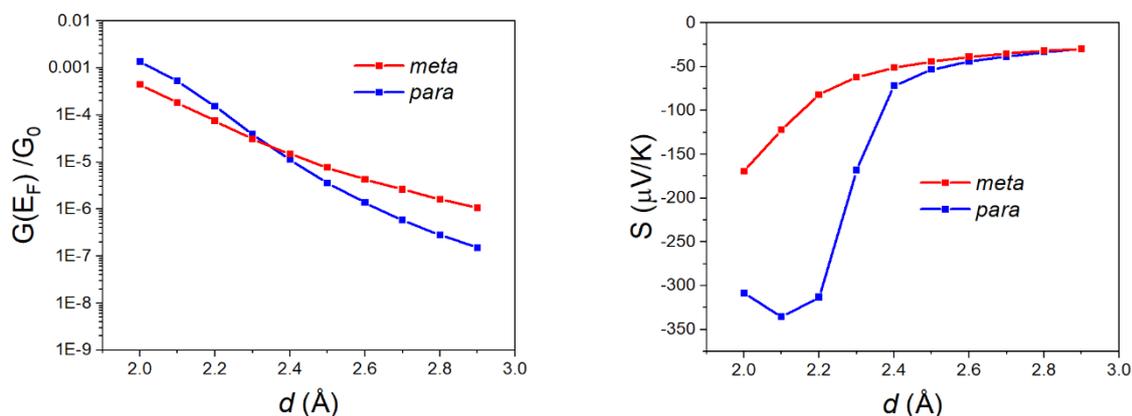
Fig. S52 X = C=O in a linear geometry. (Left) Conductance vs contact distance *d*. (Right) Seebeck coefficient against contact distance *d*.
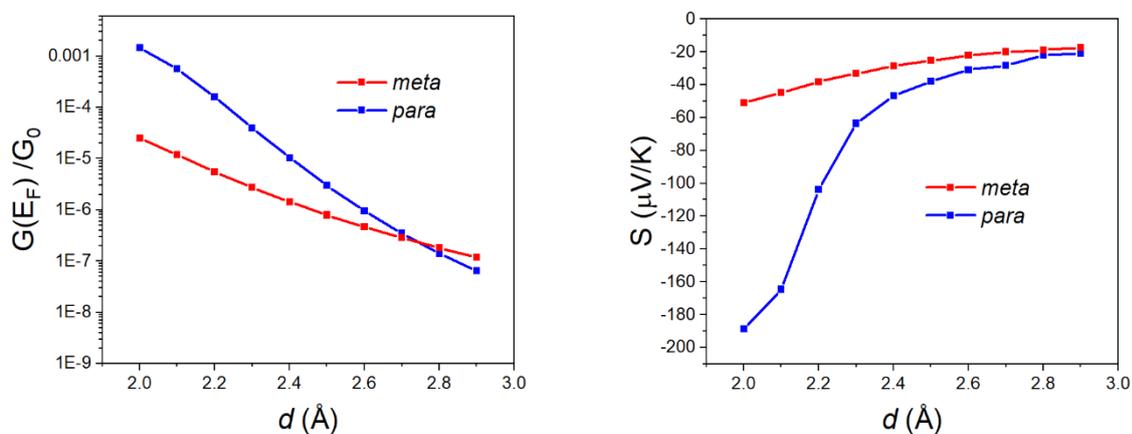
Fig. S53 X=SO_2 in a linear geometry. (Left panel) Conductance vs contact distance *d*. (Right panel) Seebeck coefficient against contact distance *d*.

Contact angle dependence

For the linear geometry, we examine how the contact angle θ (figure S54) the molecule forms in the junction controls the conductance and Seebeck coefficient.
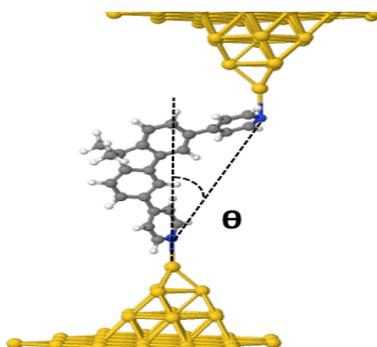
Fig. S54 Geometry of the molecule junction for varying the contact angle θ for a fixed contact distance *d*=2.5Å.

21
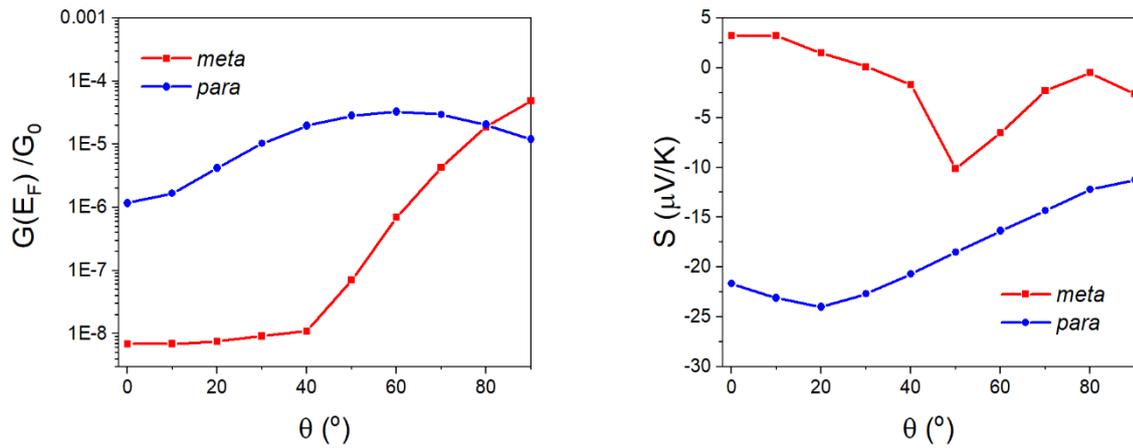
Fig. S55 Conductance (left panel) and Seebeck coefficient (right panel) as a function of tilt angle θ for **X** = CH$_2$ in a linear geometry.
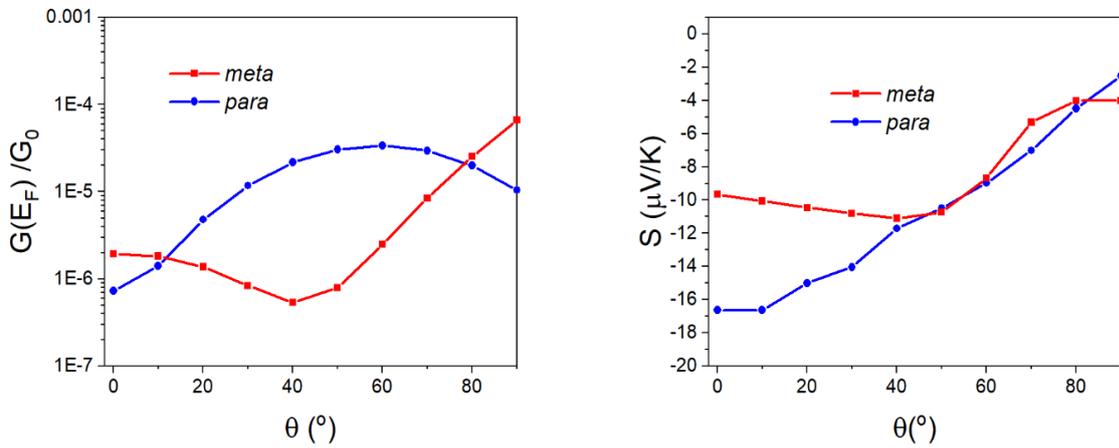
Fig. S56 Conductance (left panel) and Seebeck coefficient (right panel) as a function of tilt angle θ for **X** = S in a linear geometry.
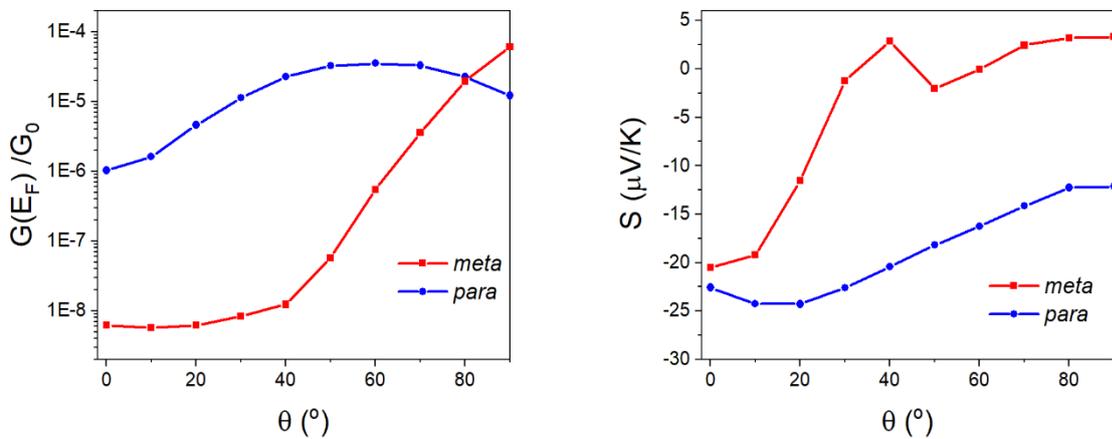
Fig. S57 Conductance (left panel) and Seebeck coefficient (right panel) as a function of tilt angle θ for **X** = CMe$_2$ in a linear geometry.
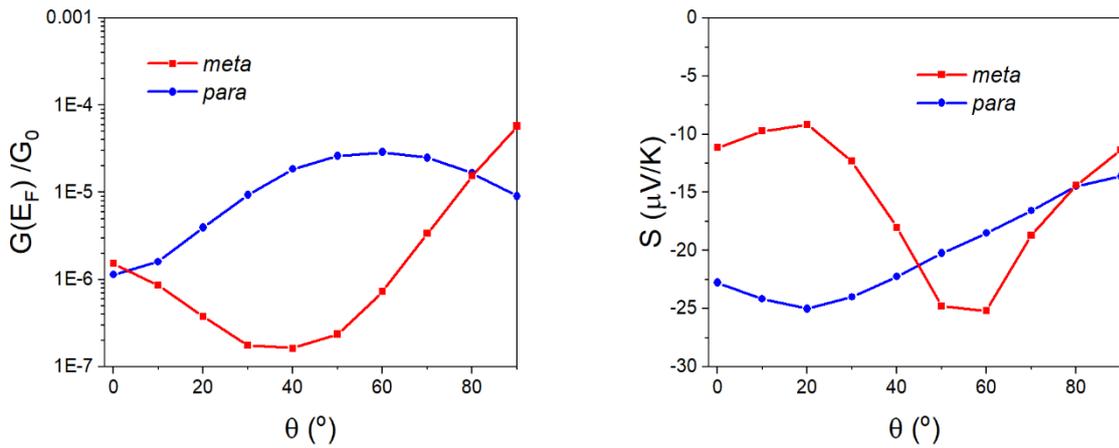
Fig. S58 Conductance (left panel) and Seebeck coefficient (right panel) as a function of tilt angle θ for **X** = O in a linear geometry.
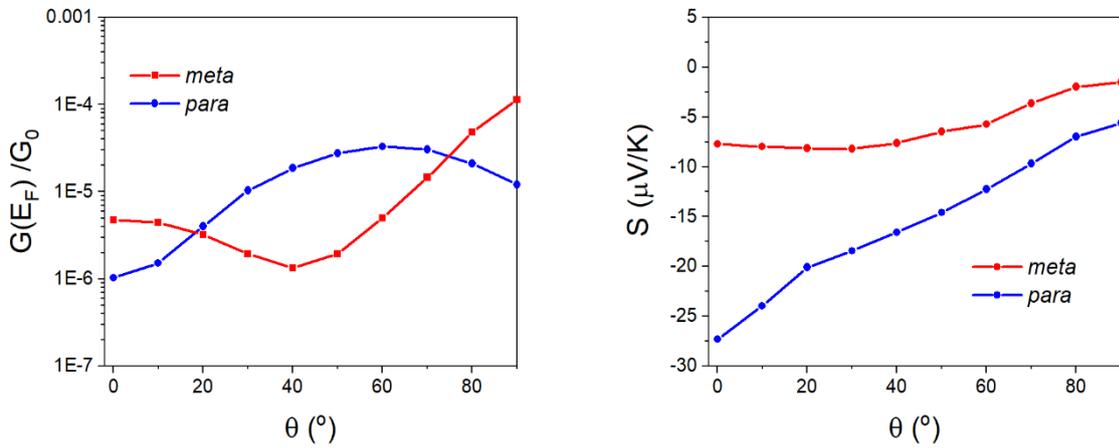
Fig. S59 Conductance (left panel) and Seebeck coefficient (right panel) as a function of tilt angle θ for **X** = NEt in a linear geometry.
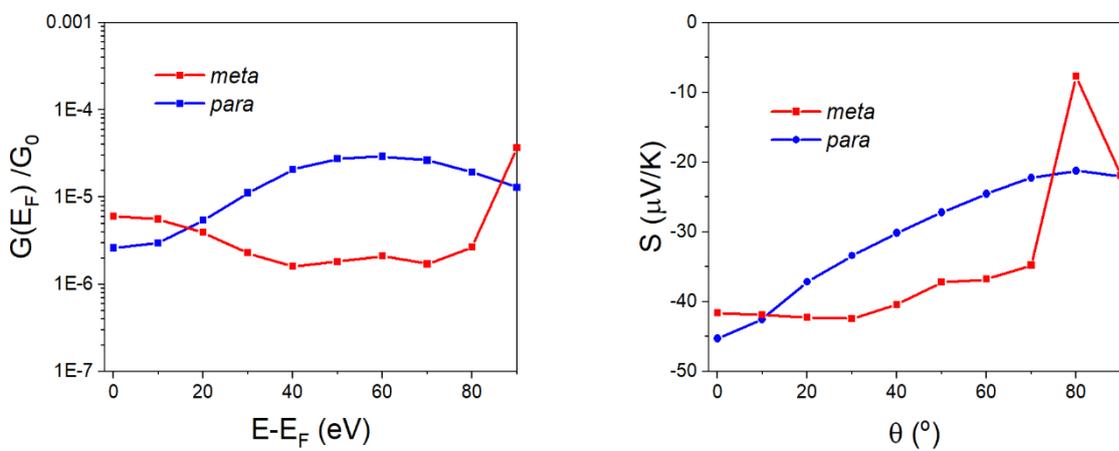
Fig. S60 Conductance (left panel) and Seebeck coefficient (right panel) as a function of tilt angle θ for **X** = C=O in a linear geometry.

23
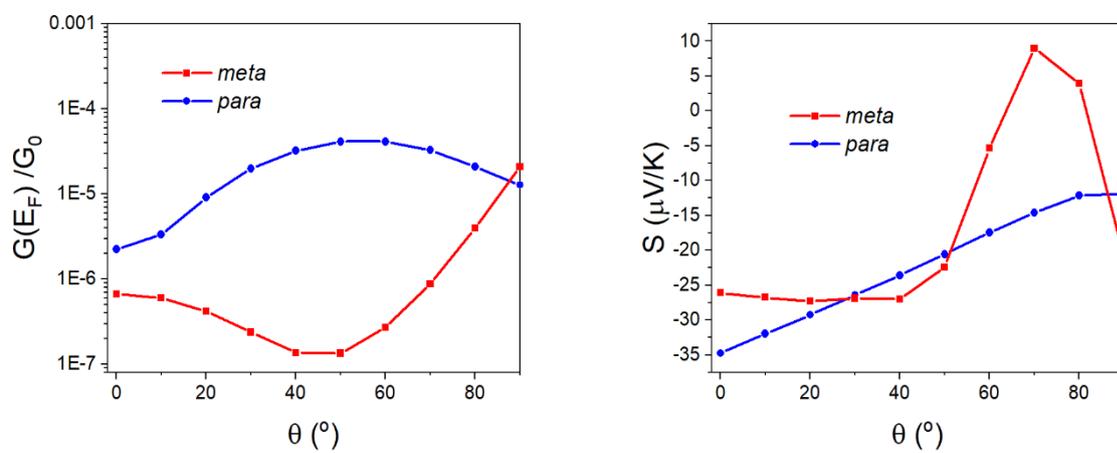
Fig. S61 Conductance (left panel) and Seebeck coefficient (right panel) as a function of tilt angle θ for **X** = SO$_2$ in a linear geometry.

S4. Molecule synthesis and charecterization

S4.1 Synthetic experimental

General: Commercial chemicals were procured from Fluorochem, Acros Organics, Sigma Aldrich, Tokyo Chemical Industry or Alfa Aesar and used as received. Anhydrous solvents were obtained from a solvent purification system. Silica gel from Fluorochem was used to perform column chromatography. ^{1}H-NMR spectra were recorded on Bruker Avance-400 MHz instruments reporting chemical shifts referenced to residual CHCl$_3$ solvent peak (δ 7.26 ppm). ^{13}C NMR (100 MHz) spectral data were collected on Bruker Avance-400 MHz instruments and chemical shifts are referenced to CDCl$_3$ solvent peak (δ 77.16 ppm). High resolution mass spectrometry was carried out on a Waters LCT Premier XE spectrometer using ASAP ionisation. The Elemental Microanalysis Service of Durham University (UK) performed the elemental analysis using an Exeter CE-400 Elemental Analyzer. Melting points were measured uncorrected using 1 °C/min heating rate on a Stuart SMP40 melting point apparatus. UV-Visible absorption spectra were recorded using a UV-Visible spectrophotometer Evolution 220 from Thermo Scientific at room temperature 10 μM in DCM.

S4.1.1 Synthesis of 3,6-dibromo-9*H*-fluorene (1a)
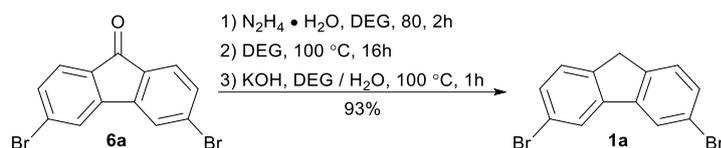
To a solution of 3,6-dibromo-9*H*-fluoren-9-one **6a** (780 mg, 2.31 mmol) in diethylene glycol (50 mL) N$_2$H$_4$·H$_2$O (1.5 mL, 1.55 g, 30.92 mmol) was added and then heated to 80 °C for 2 h and then to 100 °C overnight. The reaction was then added to KOH (980 mg, 17.47 mmol) dissolved in H$_2$O (5 mL) under continued heating for 1 h, and then poured into H$_2$O (100 mL) leading to precipitation of crude **1a** which was filtered off. The product was purified by column chromatography on silica gel using 1:1 mixture of hexane and CH$_2$Cl$_2$ as eluent. The product **1a** was isolated as a white crystalline solid (694 mg, 93%).

^{1}H-NMR (400 MHz, CDCl$_3$): δ 7.87 (2H, dd, *J* = 1.8, 0.8 Hz), 7.45 (2H, dd, J = 8.0, 1.8 Hz), 7.40 (2H, apparent dq, J = 8.0, 0.8 Hz), 3.80 (2H, s).
MS (ESI): 321.9 (M$^+$), 323.9 (M$^+$+2), 325.9 (M$^+$+4) m/z.

S4.1.2 Synthesis of 3,6-dibromo-9,9-dimethyl-9*H*-fluorene (3a)
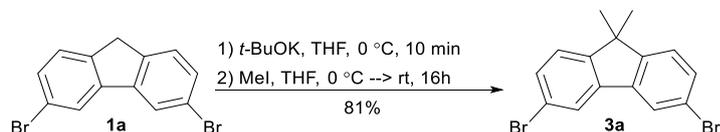
A solution of **1a** (300 mg, 0.93 mmol) in anhydrous THF (25 mL) was cooled to 0 °C. Then potassium *tert*-butoxide (554 mg, 4.94 mmol) was added, the reaction was stirred for 10 min before methyliodide (1 mL, 2.28 g, 16.06 mmol) was added and the reaction mixture was allowed to heat to rt overnight under argon. The reaction mixture was added to H$_2$O (100 mL) and extracted with CH$_2$Cl$_2$ (3×50 mL) dried over MgSO$_4$ and the solvent evaporated to dryness. The crude mixture was purified by column chromatography on silica gel using hexane as eluent. The product **3a** was isolated as a white crystalline solid (266 mg, 81%)

25

^{1}H-NMR (400 MHz, CDCl$_3$): δ 7.82 (dd, J = 1.8, 0.5 Hz, 2H), 7.47 (dd, J = 8.1, 1.8 Hz, 2H), 7.32 (dd, J = 8.1, 0.5 Hz, 2H), 1.47 (s, 6H).
MS: 349.9 (M$^+$), 351.9 (M$^+$+2), 353.9 (M$^+$+4) m/z.

S4.1.3 Synthesis of 3,6-di(pyridin-4-yl)-9H-fluorene (1)
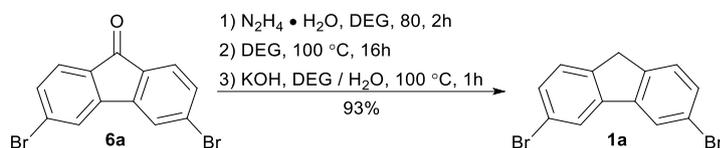
A solution of 3,6-dibromo-9H-fluorene **1a** (202 mg, 0.62 mmol), 4-pyridinylboronic acid (342 mg, 2.78 mmol) and sodium carbonate (405 mg, 3.82 mmol) in a 1:2 mixture of H$_2$O and dimethoxyethane (50 mL) was thoroughly degassed and then Pd(PPh$_3$)$_4$ (215 mg, 0.186 mmol) was added and the mixture was heated to reflux overnight. The mixture was then extracted with CH$_2$Cl$_2$ (2×50 mL), washed with H$_2$O (100 mL), dried over MgSO$_4$ and the solvent evaporated to dryness. The crude product was purified by column chromatography on silica gel using EtOAc as initial eluent and 10% MeOH in CH$_2$Cl$_2$ as secondary eluent. The product **1** was isolated as a white crystalline solid (120 mg, 60%) and was further purified by recrystallization from toluene/hexane for final measurements and analysis.

^{1}H-NMR (400 MHz, CDCl$_3$): δ 8.70 (dd, J = 4.5, 1.6 Hz, 4H), 8.11 (d, J = 1.3 Hz, 2H), 7.69 (dd, J = 7.8, 0.9 Hz, 2H), 7.65 – 7.60 (m, 8H), 4.03 (s, 2H).
^{13}C NMR (101 MHz, CDCl$_3$): δ 150.36, 148.76, 144.64, 142.25, 137.41, 126.34, 125.94, 121.96, 118.66, 36.83.
HRMS (ASAP, m/z): 321.1388 Calculated for M+H$^+$ (C$_{23}$H$_{17}$N$_2^+$): 321.1386 m/z.
Elemental analysis (CHN): C: 85.95 %, 4.97 %, 8.63 % Calculated for (C$_{23}$H$_{16}$N$_2$) C: 86.22 %, H: 5.03 %, N: 8.74 %.
Melting Point: 196.6 °C (decomposes).

S4.1.4 Synthesis of 2,8-di(pyridin-4-yl)dibenzo[b,d]thiophene (2)
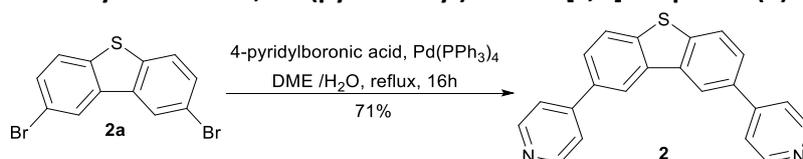
A solution of 2,8-dibromodibenzo[b,d]thiophene **2a** (1.0 g, 2.92 mmol), 4-pyridinylboronic acid (1.24 g, 10.09 mmol) and sodium carbonate (1.52 g, 14.34 mmol) in a 1:2 mixture of H$_2$O and dimethoxyethane (50 mL) was thoroughly degassed and then Pd(PPh$_3$)$_4$ (346 mg, 0.299 mmol) was added and the mixture was heated to reflux overnight. The mixture was then extracted with CH$_2$Cl$_2$ (2×50 mL), washed with H$_2$O (100 mL), dried over MgSO$_4$ and the solvent evaporated to dryness. The crude mixture was purified by column chromatography on silica gel using EtOAc as initial eluent and 10% MeOH in CH$_2$Cl$_2$ as secondary eluent. The product **2** was isolated as white with a tint of yellow crystalline solid (700 mg, 71%) and was further purified by recrystallization from toluene/hexane for final measurements and analysis.

^{1}H-NMR (400 MHz, CDCl$_3$): δ 8.73 (dd, J = 4.5, 1.6 Hz, 4H), 8.47 (dd, J = 1.8, 0.6 Hz, 2H), 8.00 (dd, J = 8.4, 0.6 Hz, 2H), 7.78 (dd, J = 8.3, 1.8 Hz, 2H), 7.66 (dd, J = 4.5, 1.6 Hz, 4H).

^{13}C NMR (101 MHz, CDCl$_3$): δ 150.50, 148.31, 140.99, 136.12, 135.18, 126.19, 123.83, 121.97, 120.22.

HRMS (ASAP, m/z): 339.0957 Calculated for M+H$^+$ (C$_{22}$H$_{15}$N$_2$S$^+$): 339.0956 m/z.

Elemental analysis (CHN): C: 77.87 %, 4.16 %, 7.95 % Calculated for (C$_{22}$H$_{14}$N$_2$S) C: 78.08 %, H: 4.17 %, N: 8.28 %.

Melting Point: 240.8 – 242.2 °C.

S4.1.5 Synthesis of 4,4'-(9,9-dimethyl-9*H*-fluorene-3,6-diyl)dipyridine (3)
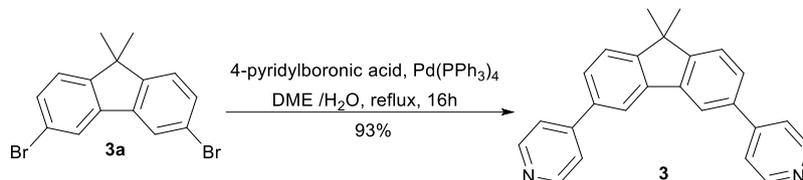
A solution of 3,6-dibromo-9,9-dimethyl-9*H*-fluorene **3a** (265 mg, 0.753 mmol), 4-pyridinylboronic acid (318 mg, 2.58 mmol) and sodium carbonate (378 mg, 3.56 mmol) in a 1:2 mixture of H$_2$O and dimethoxyethane (50 mL) was thoroughly degassed and then Pd(PPh$_3$)$_4$ (195 mg, 0.168 mmol) was added and the mixture was heated to reflux overnight. The mixture was then extracted with CH$_2$Cl$_2$ (2×50 mL), washed with H$_2$O (100 mL), dried over MgSO$_4$ and the solvent evaporated to dryness. The crude mixture was purified by column chromatography on silica gel using EtOAc as initial eluent and 10% MeOH in CH$_2$Cl$_2$ as secondary eluent. The product **3** was isolated as white crystalline solid (245 mg, 93 %) and was further purified by recrystallization from toluene/hexane for final measurements and analysis.

^{1}H-NMR (400 MHz, CDCl$_3$): δ 8.73 (dd, J = 4.5, 1.8 Hz, 4H), 8.08 (dd, J = 1.7, 0.7 Hz, 2H), 7.66 (dd, J = 7.8, 1.7 Hz, 2H), 7.63 (dd, J = 4.4, 1.7 Hz, 4H), 7.61 (dd, J = 7.8, 0.7 Hz, 2H), 1.60 (s, 6H).

^{13}C NMR (101 MHz, CDCl$_3$): δ 154.85, 150.20, 148.67, 139.60, 137.50, 126.80, 123.44, 121.83, 118.74, 46.93, 27.04.

HRMS (ASAP, m/z): 349.1704 Calculated for M+H$^+$ (C$_{26}$H$_{21}$N$_2$$^+$): 349.1705 m/z.

Elemental analysis (CHN): C: 85.91 %, 6.00 %, 7.50 % Calculated for (C$_{26}$H$_{20}$N$_2$) C: 86.17 %, H: 5.79 %, N: 8.04 %.

Melting Point: 227.7 – 228.5 °C.

S4.1.6 Synthesis of 2,8-di(pyridin-4-yl)dibenzo[b,d]furan (4)

A solution of 3,6-dibromodibenzo[*b,d*]furan 4**a** (520 mg, 1.60 mmol), 4-pyridinylboronic acid (605 mg, 4.92 mmol) and sodium carbonate (635 mg, 5.99 mmol) in a 1:2 mixture of H$_2$O and dimethoxyethane (50 mL) was thoroughly degassed and then Pd(PPh$_3$)$_4$ (245 mg, 0.212 mmol) was added and the mixture was heated to reflux overnight. The mixture was then extracted with CH$_2$Cl$_2$ (2×50 mL), washed with H$_2$O (100 mL), dried over MgSO$_4$ and the solvent evaporated to dryness. The crude mixture was purified by column chromatography on silica gel using EtOAc as initial eluent and 10% MeOH in CH$_2$Cl$_2$ as secondary eluent. The product **4** was isolated as a white crystalline solid (389 mg, 76%) and was further purified by recrystallization from toluene/hexane for final measurements and analysis.

^{1}H-NMR (400 MHz, CDCl$_3$): δ 8.71 (dd, J = 4.6, 1.5 Hz, 4H), 8.27 (dd, J = 2.0, 0.6 Hz, 2H), 7.78 (dd, J = 8.6, 1.9 Hz, 2H), 7.71 (dd, J = 8.6, 0.7 Hz, 2H), 7.61 (dd, J = 4.4, 1.6 Hz, 4H).

^{13}C NMR (101 MHz, CDCl$_3$): δ 157.04, 150.10, 148.11, 133.41, 126.70, 124.61. 121.69, 119.26, 112.38.

HRMS (ASAP, m/z): 323.1172 Calculated for M+H$^+$ (C$_{22}$H$_{15}$N$_2$O$^+$): 323.1184 m/z.

Elemental analysis (CHN): C: 81.80 %, 4.43 %, 8.40 % Calculated for (C$_{22}$H$_{14}$N$_2$O) C: 81.97 %, H: 4.38 %, N: 8.69 %.

Melting Point: 249.8 – 252.3 °C.

S4.1.7 Synthesis of 9-ethyl-3,6-di(pyridin-4-yl)-9*H*-carbazole (5)

A solution of 3,6-dibromo-9-ethyl-9*H*-carbazole 5**a** (1.01 g, 2.86 mmol), 4-pyridinylboronic acid (1.042 g, 8.48 mmol) and sodium carbonate (1.209 g, 11.4 mmol) in a 1:2 mixture of H$_2$O and dimethoxyethane (50 mL) was thoroughly degassed and then Pd(PPh$_3$)$_4$ (251 mg, 0.251 mmol) was added and the mixture was heated to reflux overnight. The mixture was then extracted with CH$_2$Cl$_2$ (2×50 mL), washed with H$_2$O (100 mL), dried over MgSO$_4$ and the solvent evaporated to dryness. The crude mixture was purified by column chromatography on silica gel using EtOAc as initial eluent and 10% MeOH in CH$_2$Cl$_2$ as secondary eluent. The product **5** was isolated as a slightly yellowish white crystalline solid (690 mg, 69%) and was further purified by recrystallization from toluene/hexane for final measurements and analysis.

^{1}H-NMR (400 MHz, CDCl$_3$): δ 8.68 (dd, J = 4.6, 1.7 Hz, 4H), 8.46 (dd, J = 1.8, 0.6 Hz, 2H), 7.82 (dd, J = 8.6, 1.8 Hz, 2H), 7.67 (dd, J = 4.6, 1.6 Hz, 4H), 7.54 (dd, J = 8.6, 0.6 Hz, 2H), 4.45 (q, J = 7.2 Hz, 2H), 1.51 (t, J = 7.2 Hz, 3H).

^{13}C NMR (101 MHz, CDCl$_3$): δ 150.13, 149.29, 141.12, 129.50, 125.45, 123.76, 121.77, 119.35, 109.60, 38.15, 14.04.

HRMS (ASAP, m/z): 350.1662 Calculated for M+H$^+$ (C$_{24}$H$_{20}$N$_3$$^+$): 350.1657 m/z.
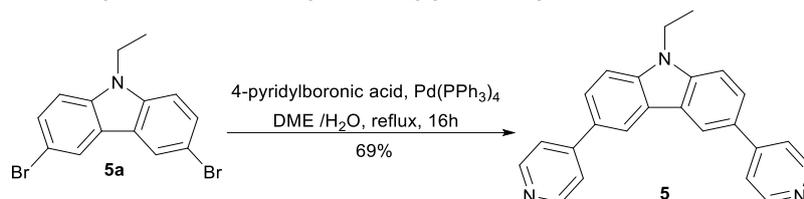
Elemental analysis (CHN): C: 82.77 %, 5.34 %, 11.89 % Calculated for (C$_{26}$H$_{20}$N$_2$) C: 82.49 %, H: 5.48 %, N: 12.03 %.

Melting Point: 242.2 – 244.3 °C.

S4.1.8 Synthesis of 3,6-di(pyridin-4-yl)-9*H*-fluoren-9-one (6)
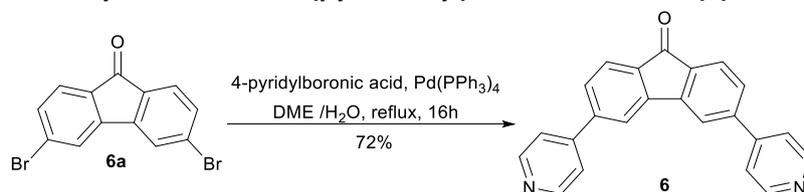
A solution of 3,6-dibromo-9*H*-fluoren-9-one **6a** (520 mg, 0.947 mmol), 4-pyridinylboronic acid (345 mg, 2.81 mmol) and sodium carbonate (425 mg, 4.01 mmol) in a 1:2 mixture of H$_2$O and dimethoxyethane (50 mL) was thoroughly degassed and then Pd(PPh$_3$)$_4$ (205 mg, 0.178 mmol) was added and the mixture was heated to reflux overnight. The mixture was then extracted with CH$_2$Cl$_2$ (2×50 mL), washed with H$_2$O (100 mL), dried over MgSO$_4$ and the solvent evaporated to dryness. The crude mixture was purified by column chromatography on silica gel using EtOAc as initial eluent and

10% MeOH in CH$_2$Cl$_2$ as secondary eluent. The product **6** was isolated as yellow crystalline solid (229 mg, 72%) and was further purified by recrystallization from toluene/hexane for final measurements and analysis.

^{1}H-NMR (400 MHz, CDCl$_3$): δ 8.75 (dd, J = 4.5, 1.6 Hz, 4H), 7.86 (dd, J = 1.6, 0.7 Hz, 2H), 7.82 (dd, J = 7.7, 0.6 Hz, 2H), 7.62 (dd, J = 7.7, 1.5 Hz, 2H), 7.58 (dd, J = 4.5, 1.7 Hz, 4H).
^{13}C NMR (101 MHz, CDCl$_3$): δ 192.52, 150.64, 147.43, 145.02, 144.89, 134.86, 128.68, 125.30, 121.81, 119.35.
HRMS (ASAP, m/z): 335.1191 Calculated for M+H$^+$ (C$_{23}$H$_{15}$N$_2$O$^+$): 335.1184 m/z.
Elemental analysis (CHN): C: 82.37 %, 4.48 %, 8.19 % Calculated for (C$_{23}$H$_{14}$N$_2$) C: 82.62 %, H: 4.22 %, N: 8.38 %.
Melting Point: 268.7 °C (decomposes).

S4.1.9 Synthesis of 2,8-di(pyridin-4-yl)dibenzo[*b,d*]thiophene 5,5-dioxide (7)
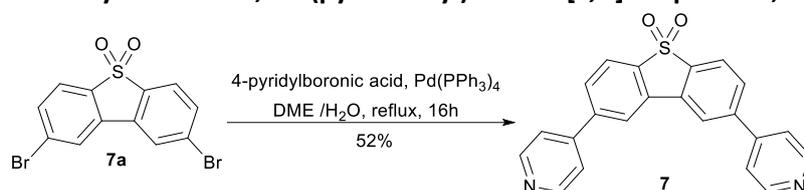
A solution of 2,8-dibromodibenzo[*b,d*]thiophene 5,5-dioxide **7a** (0.98 g, 2.62 mmol), 4-pyridinylboronic acid (1.20 g, 9.76 mmol) and sodium carbonate (1.26 g, 11.89 mmol) in a 1:2 mixture of H$_2$O and dimethoxyethane (50 mL) was thoroughly degassed and then Pd(PPh$_3$)$_4$ (300 mg, 0.260 mmol) was added and the mixture was heated to reflux overnight. The mixture was then extracted with CH$_2$Cl$_2$ (2×50 mL), washed with H$_2$O (100 mL), dried over MgSO$_4$ and the solvent evaporated to dryness. The crude mixture was purified by column chromatography on silica gel using EtOAc as initial eluent and 10% MeOH in CH$_2$Cl$_2$ as secondary eluent. The product **7** was isolated as white crystalline solid (508 mg, 52 %) and was further purified by recrystallization from toluene/hexane for final measurements and analysis.

^{1}H-NMR (400 MHz, CDCl$_3$): δ 8.81 – 8.75 (m, 4H), 8.09 (d, J = 1.6 Hz, 2H), 7.98 (d, J = 7.9 Hz, 2H), 7.81 (dd, J = 8.0, 1.5 Hz, 2H), 7.61 – 7.54 (m, 4H).
^{13}C NMR (101 MHz, CDCl$_3$): δ 150.87, 146.49, 144.68, 138.43, 132.30, 129.84, 123.29, 121.91, 120.49.
HRMS (ASAP, m/z): 371.0851 Calculated for M+H$^+$ (C$_{22}$H$_{15}$N$_2$O$_2$S$^+$): 371.0854 m/z.
Elemental analysis (CHN): C: 71.41 %, 3.96 %, 7.31 % Calculated for (C$_{22}$H$_{14}$N$_2$O$_2$S) C: 71.33 %, H: 3.81 %, N: 7.56 %.
Melting Point: 247.1 °C (decomposes).

S4.2 **NMR spectra**

### S4.2.1 ^{1}H NMR Spectrum of 3,6-dibromo-9H-fluorene (1a)
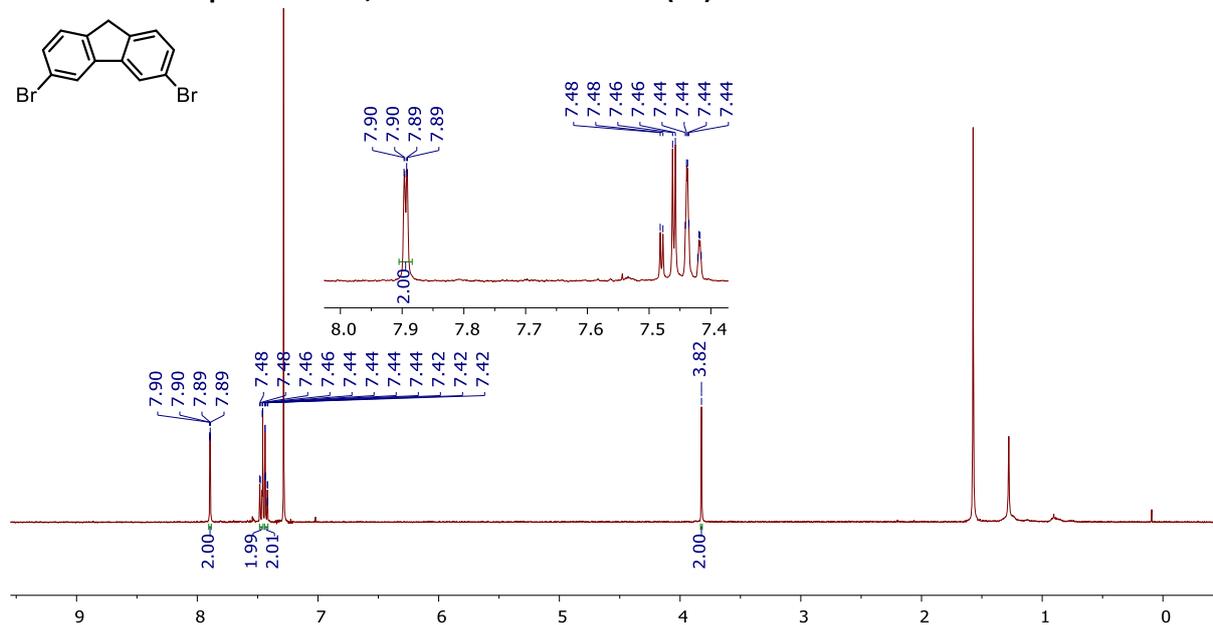
Fig. S62 ^{1}H NMR Spectrum of **1a** in CDCl$_3$ (δ 7.26 ppm)

S4.2.12 ^{1}H NMR Spectrum of 3,6-dibromo-9,9-dimethyl-9H-fluorene (3a)
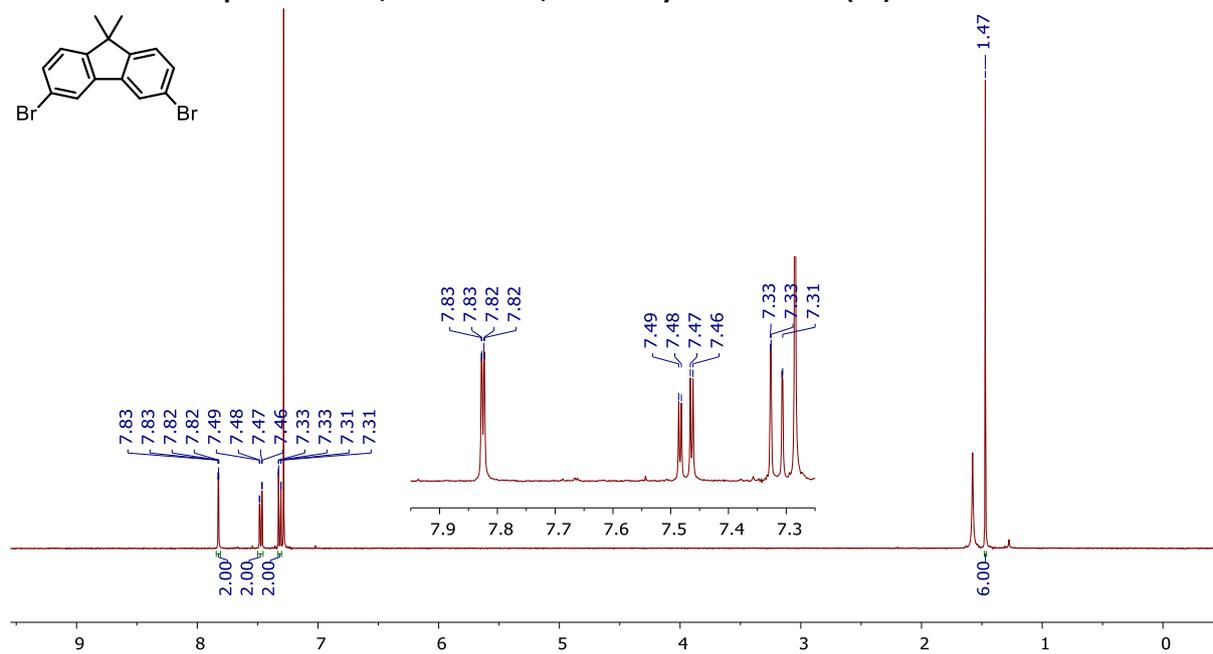
Fig. S63 ^{1}H NMR Spectrum of **3a** in CDCl$_3$ (δ 7.26 ppm)

S4.2.3 ¹H NMR and ¹³C NMR Spectra of 3,6-di(pyridin-4-yl)-9*H*-fluorene (1)
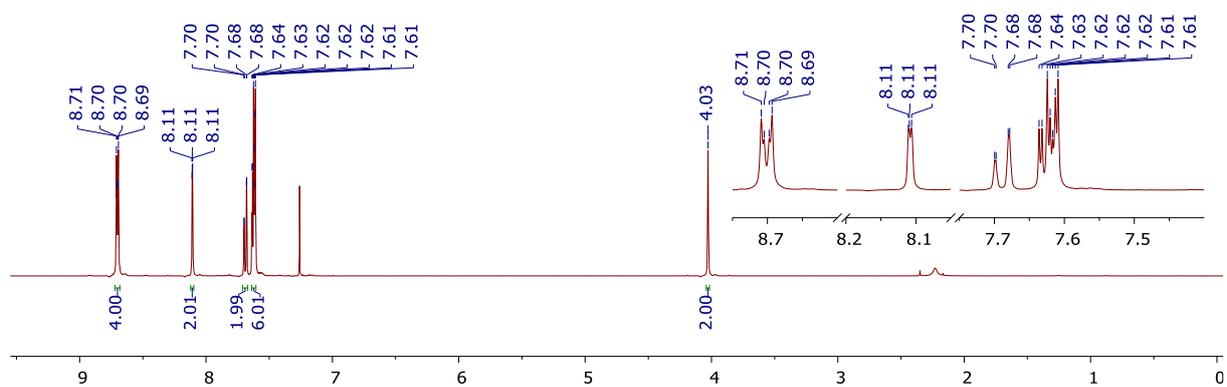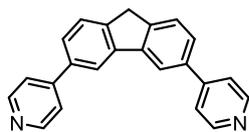
Fig. S64 ¹H NMR Spectrum of 1 in CDCl₃ (δ 7.26 ppm)

Fig.S65 ¹³C NMR Spectrum of 1 in CDCl₃ (δ 77.16 ppm)

S4.2.3 ^{1}H NMR and ^{13}C NMR Spectra of 3,6-di(pyridin-4-yl)-9*H*-fluorene (1)

Fig. S64 ^{1}H NMR Spectrum of 1 in CDCl₃ (δ 7.26 ppm)
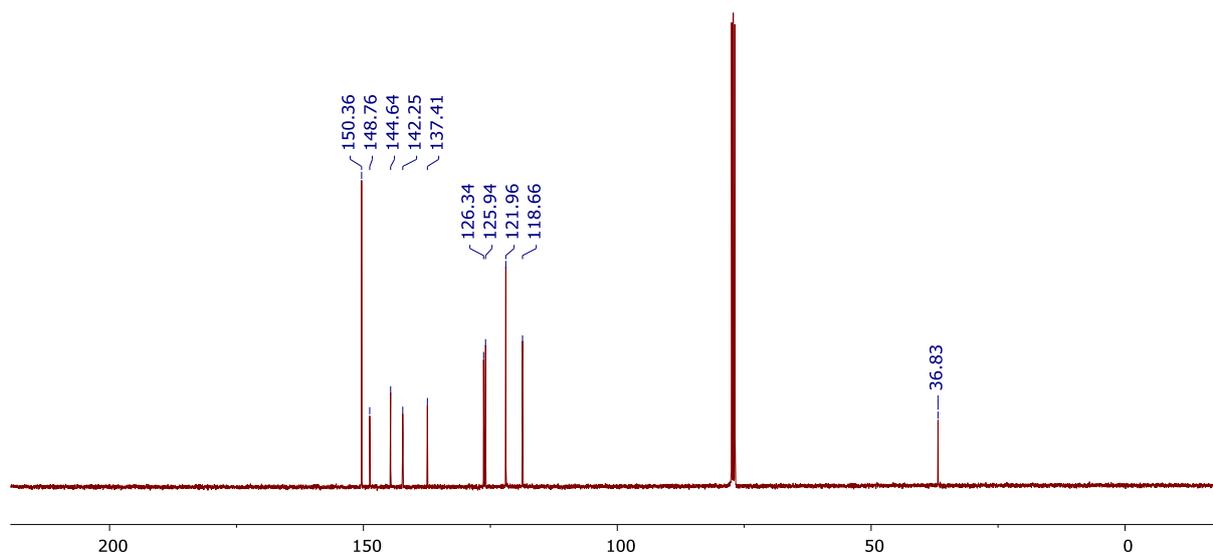
Fig.S65 ^{13}C NMR Spectrum of 1 in CDCl₃ (δ 77.16 ppm)

S4.2.4 ^{1}H NMR and ^{13}C NMR Spectra of 2,8-di(pyridin-4-yl)dibenzo[*b,d*]thiophene (2)
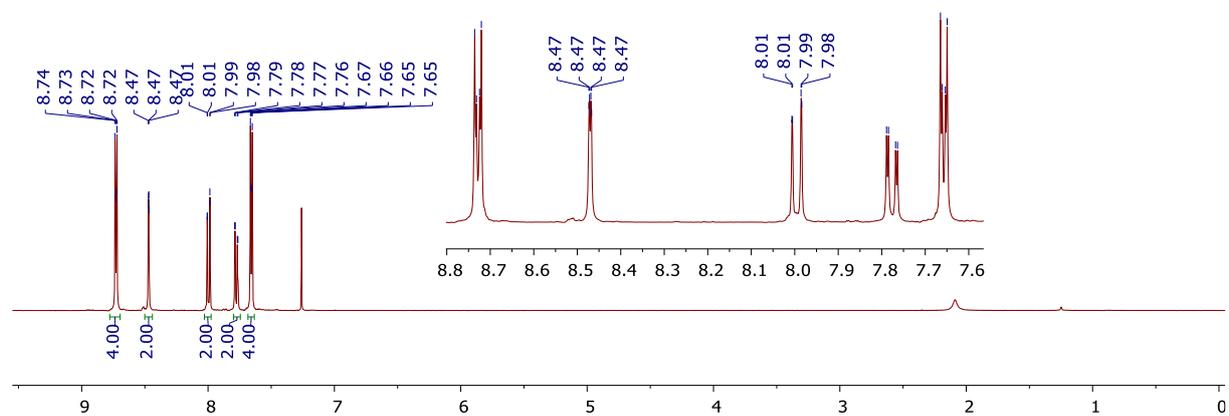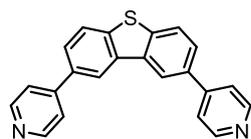
Fig. S66 ^{1}H NMR Spectrum of **2** in CDCl$_3$ (δ 7.26 ppm)
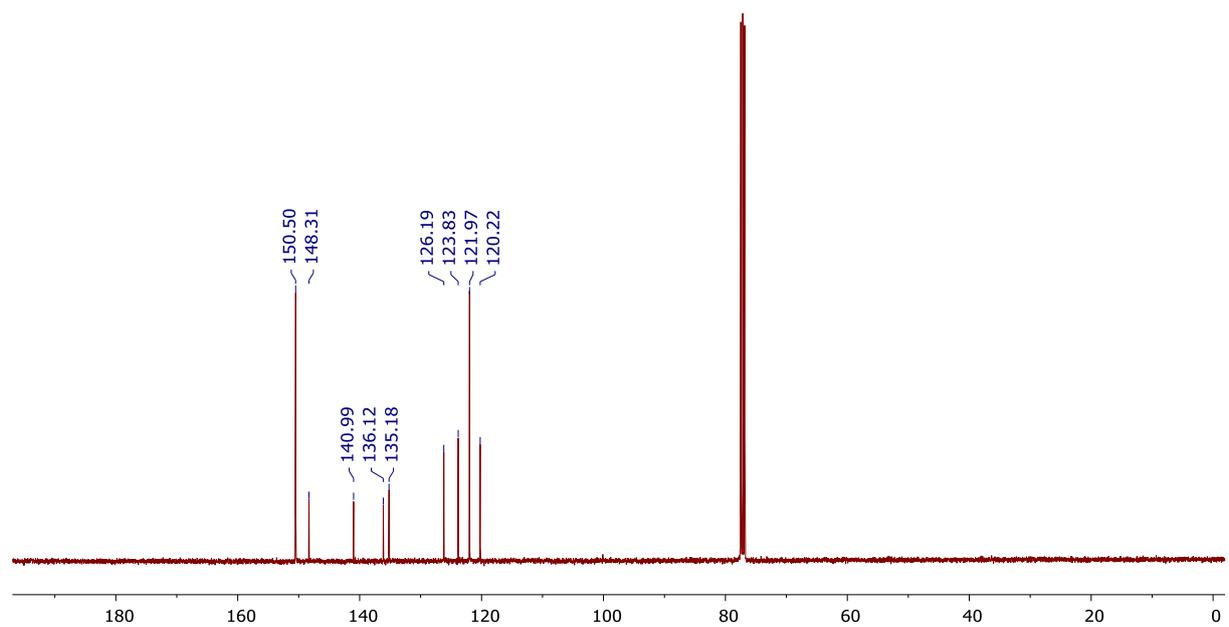
Fig. S67 ^{13}C NMR Spectrum of **2** in CDCl$_3$ (δ 77.26 ppm)

S4.2.5 ¹H NMR and ¹³C NMR Spectra of 4,4'-(9,9-dimethyl-9H-fluorene-3,6-diyl)dipyridine (5)
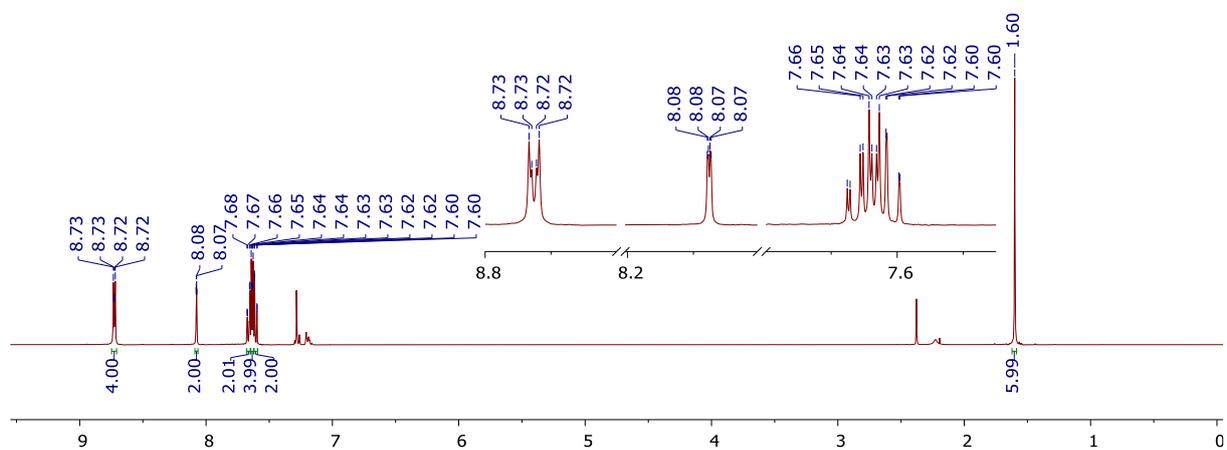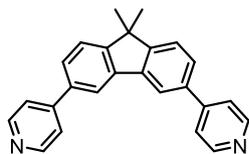
Fig. S68 ¹H NMR Spectrum of **5** in CDCl₃ (δ 7.26 ppm)
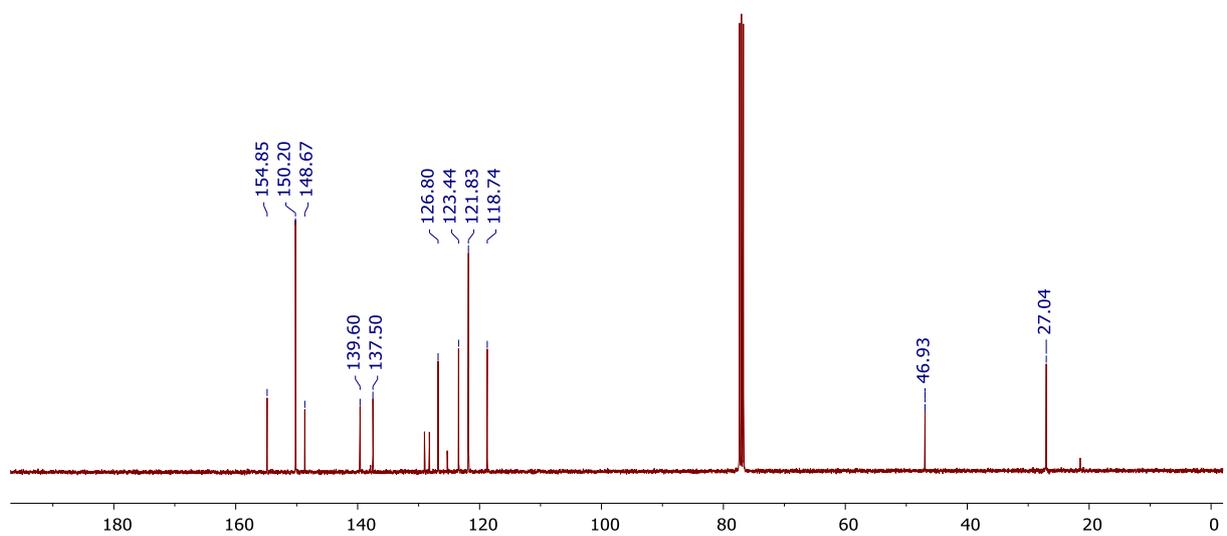
Fig. S69 ¹³C NMR Spectrum of **5** in CDCl₃ (δ 77.16 ppm)

S4.2.6 ^{1}H NMR and ^{13}C NMR Spectra of 2,8-di(pyridin-4-yl)dibenzo[b,d]furan (4)
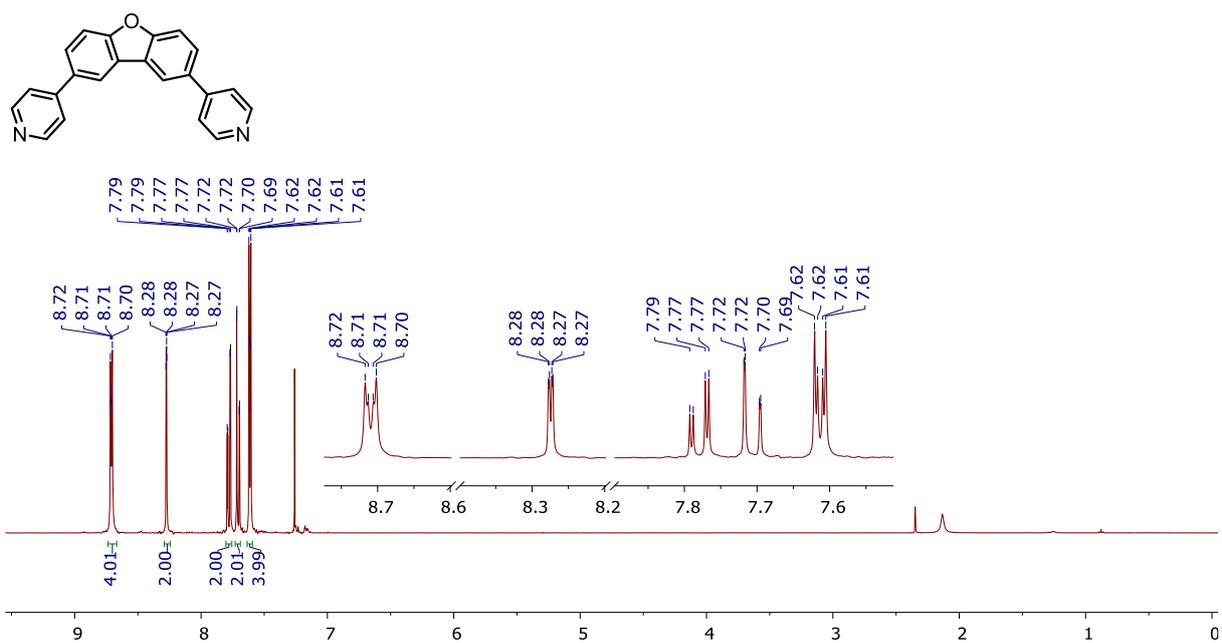
Fig. S70 ^{1}H NMR Spectrum of **4** in CDCl$_3$ (δ 7.26 ppm)
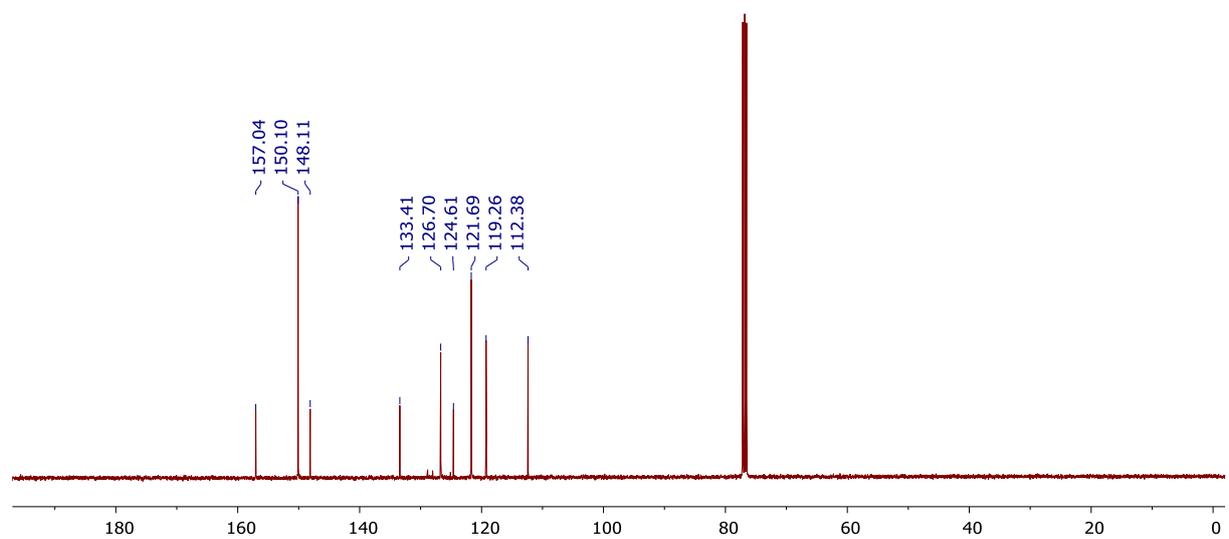
Fig. S71 ^{13}C NMR Spectrum of **4** in CDCl$_3$ (δ 77.16 ppm)

S4.2.7 ^{1}H NMR and ^{13}C NMR Spectra of 9-ethyl-3,6-di(pyridin-4-yl)-9*H*-carbazole (5)
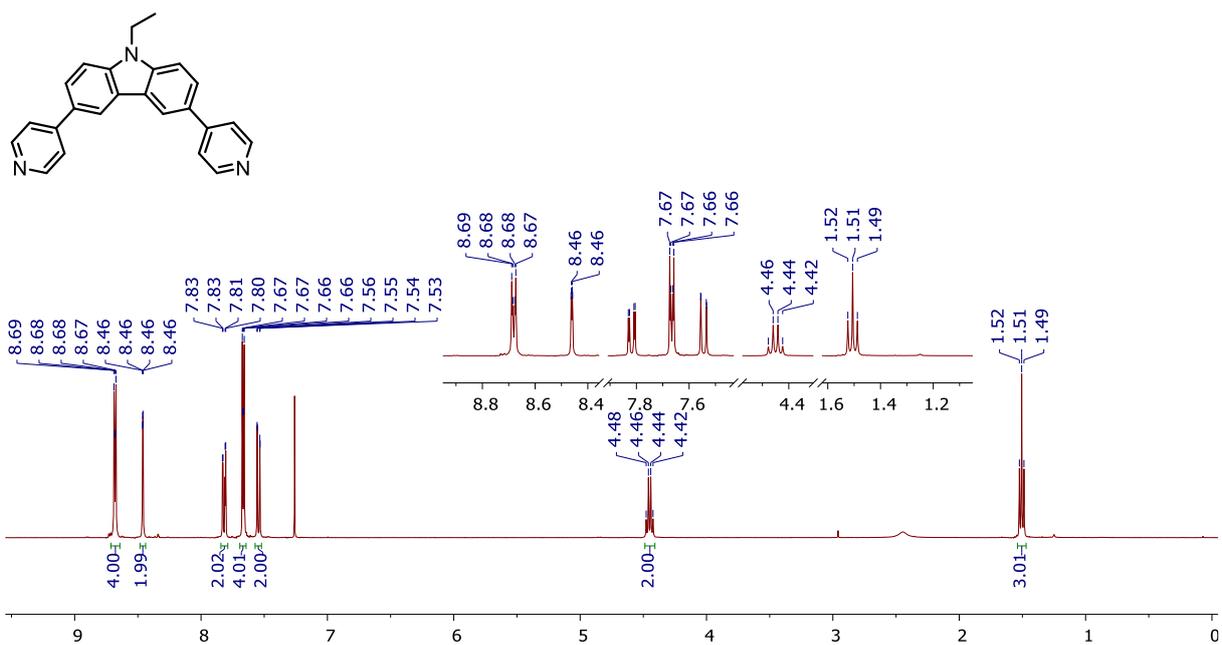
Fig. S72 ^{1}H NMR Spectrum of **5** in CDCl$_3$ (δ 7.26 ppm)
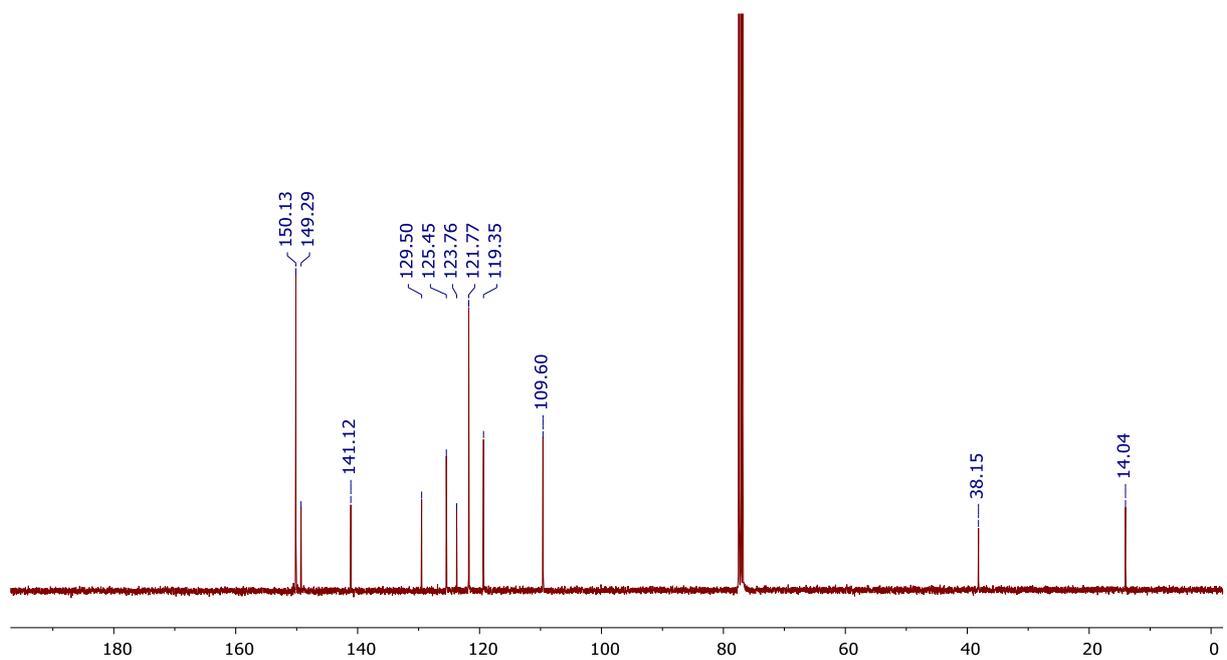
Figure S73 ^{13}C NMR Spectrum of **5** in CDCl$_3$ (δ 77.16 ppm)

S4.2.8 ^{1}H NMR and ^{13}C NMR Spectra of 3,6-di(pyridin-4-yl)-9H-fluoren-9-one (6)
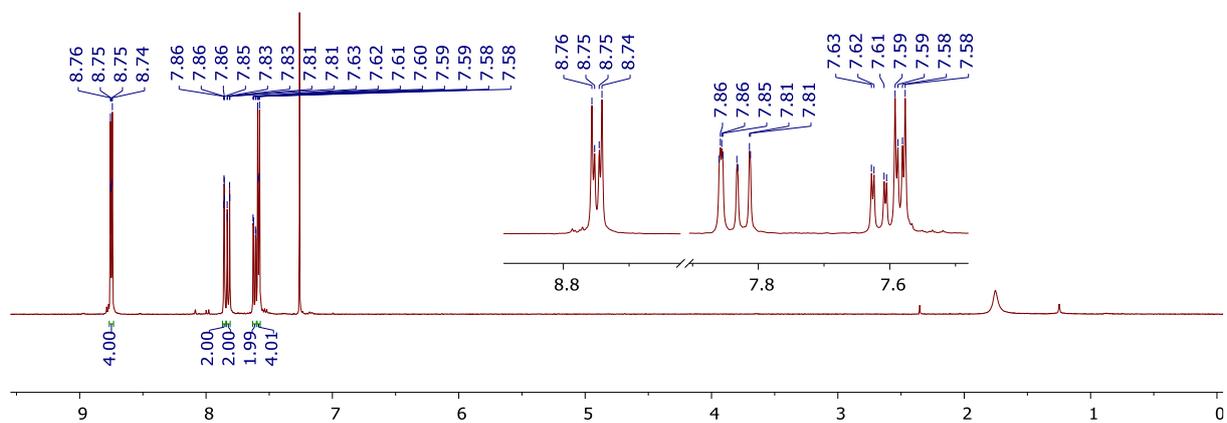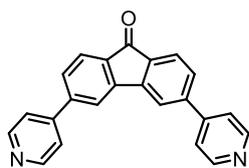
Fig. S74 ^{1}H NMR Spectrum of **6** in CDCl$_3$ (δ 7.26 ppm)
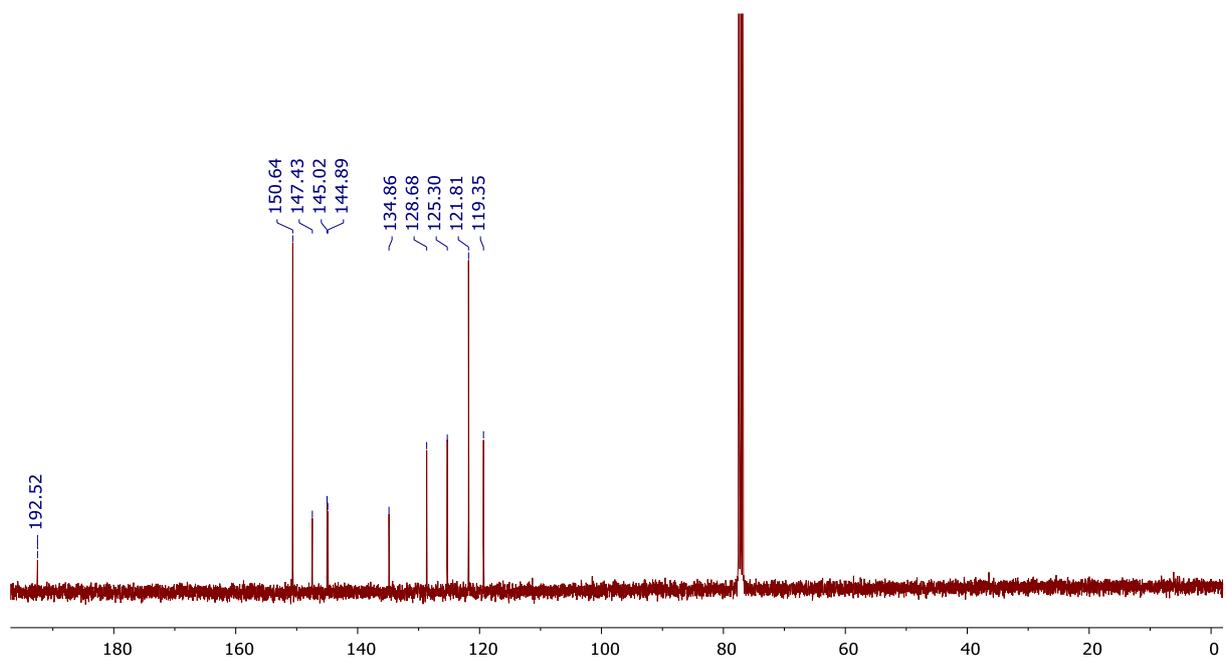
Figure S75 ^{13}C NMR Spectrum of **6** in CDCl$_3$ (δ 77.16 ppm)

S4.2.9 ^{1}H NMR and ^{13}C NMR Spectra of 2,8-di(pyridin-4-yl)dibenzo[*b,d*]thiophene 5,5-dioxide (7)
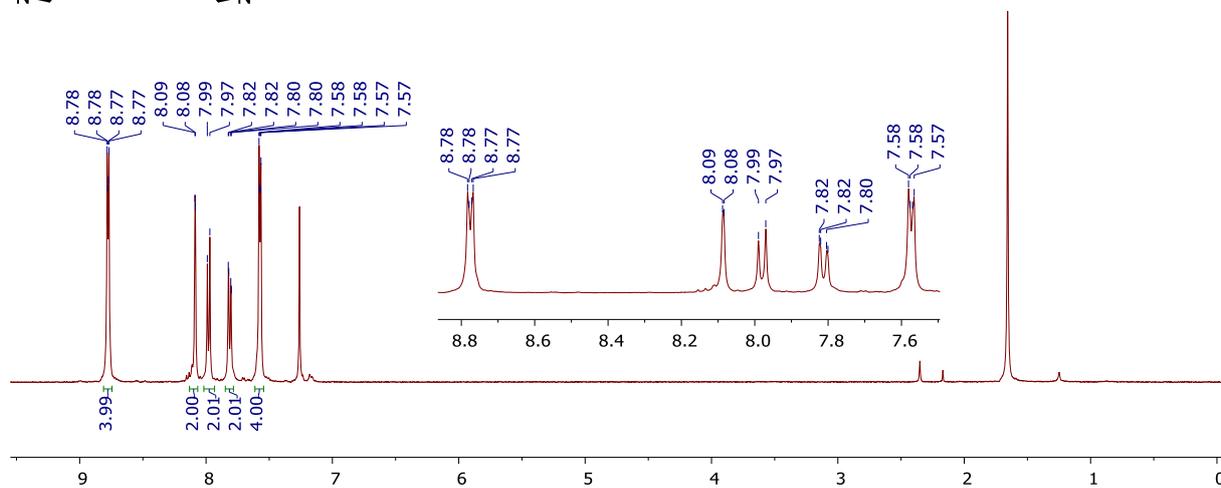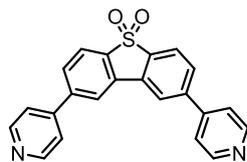
Fig. S76 ^{1}H NMR Spectrum of **7** in CDCl$_3$ (δ 7.26 ppm)
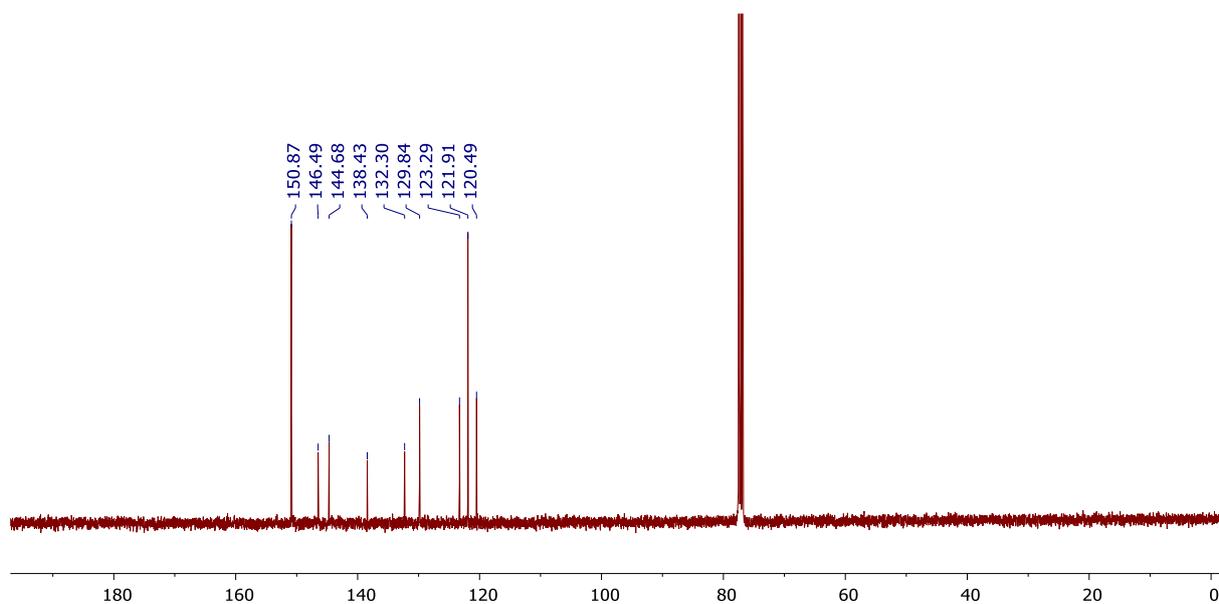
Fig. S77 ^{13}C NMR Spectrum of **7** in CDCl$_3$ (δ 77.16 ppm)

S4.3 UV-Vis spectroscopy

Room temperature absorption spectra of compounds **1-7** in dichloromethane are shown in Figure S78. Table S2 summarizes the absorptions bands λ_{max} and extinction coefficients. A pyridyl absorption band is observed at 256-276 nm; for some of the compounds this absorption is slightly red shifted compared to pyridine 256 nm[5]. In the *para* series the pyridyl absorption band is generally not observed in the spectral range (250-400 nm) due to a slight blue shift with the exception of compound **9** [**X** = C(OMe)][6]. Absorption bands assigned to the core structure are also observed at 278-342 nm; for compound **4** and **6** these are shoulder bands.
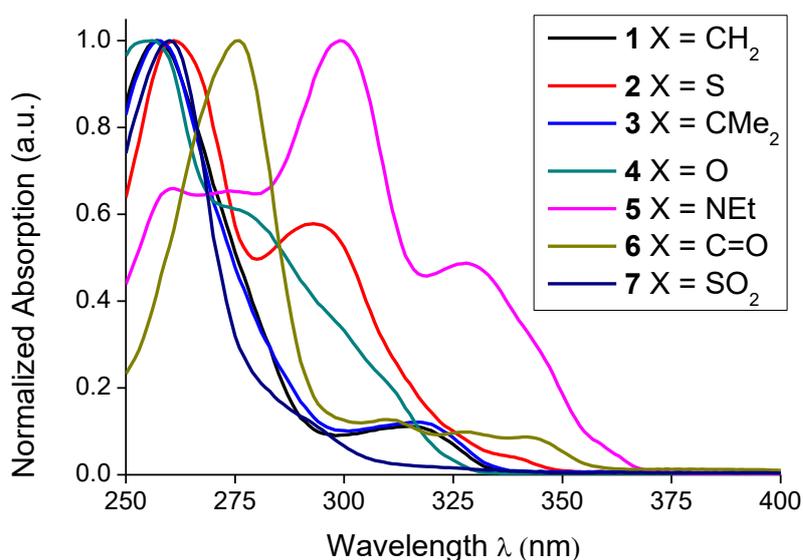
Figure S78. Normalized absorption spectra of **1-7** in dichloromethane.

	Core absorption band			Pyridyl absorption band		
	λ (nm)	A	ε (cm L mol$_{-1}$)	λ (nm)	A	ε (cm L mol$_{-1}$)
1 X = CH$_2$	278	0.295	3.0×10^4	256	0.491	4.9×10^4
2 X = S	317	0.058	5.8×10^3	257	0.480	4.8×10^4
3 X = CMe$_2$	328	0.172	1.7×10^4	261	0.233	2.3×10^4
4 X = O	293	0.311	3.1×10^4	261	0.537	5.4×10^4
5 X = NEt	315	0.048	4.8×10^3	257	0.427	4.3×10^4
6 X = C=O	292	0.068	6.8×10^3	260	0.550	5.5×10^4
7 X = SO$_2$	342	0.055	5.5×10^3	276	0.627	6.3×10^4

Table S2. Absorptions band data for compounds **1**-**7**.

S5. Conductance and thermopower measurements

S5.1 Experimental procedure

All compounds are deposited onto a pre-annealed Au (111) sample using the drop casting technique. The Au sample is annealed at approximately 900 K for $1-2$ min and allowed to cool down to room temperature; then it is introduced into a 1 mM solution of the compound for 40 min and dried with streaming nitrogen to avoid molecular clusters.

To perform the measurements, we use a home-built scanning tunneling microscope (STM) capable of measuring simultaneously the conductance, G, and the thermopower, S. The STM-Break Junction (STM-BJ) technique is used to form the single-molecule junctions at room temperature and ambient conditions, using a mechanically cut Au tip (0.25 mm diameter, 99.99% purity, Goodfellow). By indenting the STM tip into the substrate we create a Au-Au contact, initiating an IZ curve. Retracting the tip, the Au-Au monoatomic contact breaks and the single-molecule junction is sometimes formed. If the STM tip continues retracting the molecular junction is finally broken and the tunneling current goes to zero, ending the IZ curve. The bias voltage ($V_{bias} = 200$ mV) is applied to the sample and a 12 MΩ resistor is connected in series with the tip-sample junction in order to monitor the Au-Au monoatomic contact. The tunneling current is amplified using a home-built linear current-voltage ($I-V$) converter with a gain of $5 \cdot 10^8$ V/A.

To create a temperature difference between the tip and the sample (ΔT) and measure the thermopower of the molecular junctions, a 1 kΩ surface resistor is placed onto the tip holder, leaving the sample at room temperature (T_c) and heating up the tip ($T_h > T_c$). ΔT is varied between 0 K and 34 K and, for each T_h established, the system is allowed to stabilize for approximately 15 min. The temperature difference at the molecular junction creates a thermoelectric response (V_{th}) composed of a molecular contribution, $S\Delta T$, and a contribution of the copper lead that connects the tip to the rest of the setup, $-S_{lead}\Delta T$, where S and S_{lead} are the Seebeck coefficient of the molecular junction and the copper lead, respectively (see Figure S79a). Taking into account all these components, the current I through the junction is described by:

$$I = G(V_{bias} + V_{th}) = G(V_{bias} + S\Delta T - S_{lead}\Delta T), \qquad \text{Eq. (1)}$$

where G is the conductance of the junction. A scheme of this equivalent thermal-electrical circuit is shown in Figure S79a.
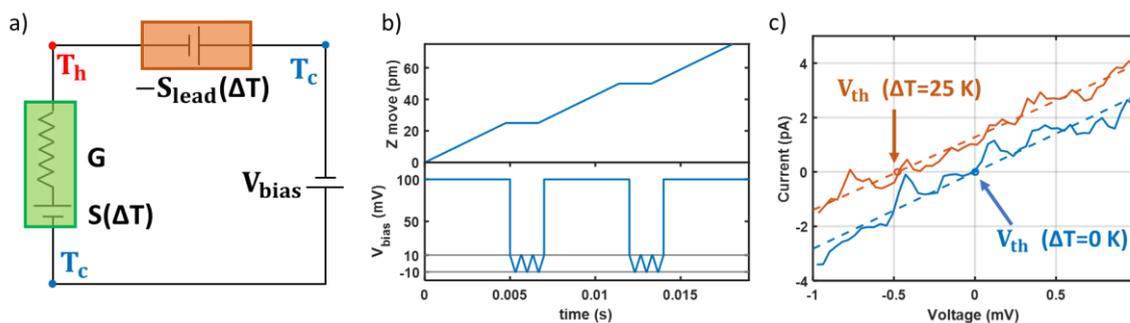
Fig. S79: a) Scheme of the equivalent thermal-electric circuit, where G and S are the conductance and Seebeck coefficient of the junction, respectively; ΔT is the difference of temperature between the tip and the sample ($\Delta T = T_h - T_c$), and S_{lead} is the Seebeck coefficient of the tip-connecting copper lead. b) Piezo movement and V_{bias} values as the junction is stretched. c) Example of two IV curves measured while the junction is stretched. V_{th} and G are obtained from the zero-current crossing point and from the slope, respectively. The example in blue is for $\Delta T = 0$ K and the red one, for $\Delta T = 25$ K.

In order to measure V_{th}, voltage ramps (IV curves) of ± 10 mV are done while the molecular junction is stretched. V_{bias} is fixed to 200 mV during the tip motion but once the molecular junction is formed, we measure three small IV ramps every 15 pm, as shown in Figure S79b,c, and then obtain the average IV curve of the three measured at the each point. From these averaged curves we obtain V_{th} from the $I = 0$ crossing point and also G from its slope (see Figure S79c). With this method several S data points can be measured in each single-molecule junction[7].

S5.2 Experimental results ordered by decreasing conductance
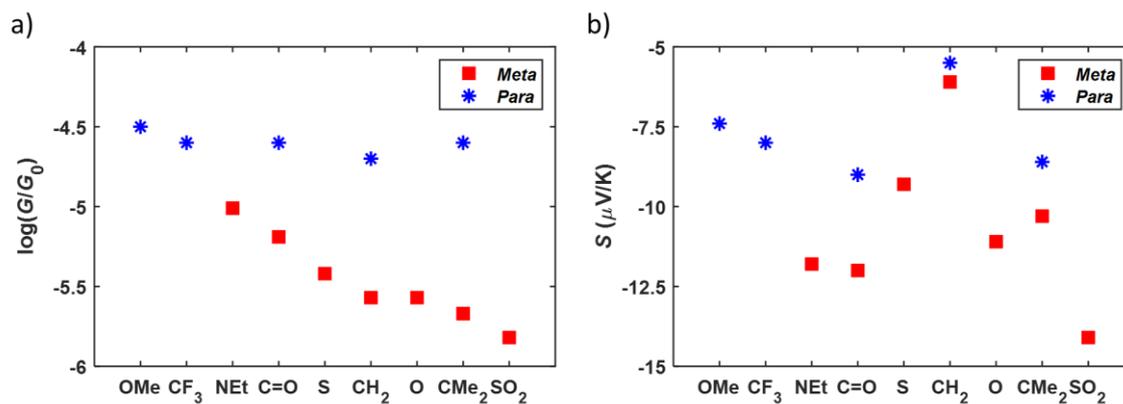
Figure S80: Measured conductance (a) and Seebeck coefficient (b) for the *meta*-connected compounds **1**-**7** (red squares), ordered by decreasing conductance, and comparison with the values of the *para*-connected systems (blue stars)[6].

## S6. Correlation study of Seebeck coefficient with other parameters

To find any underlying properties that can explain the trend of the Seebeck coefficient data and give a better understanding of how to control and manipulate it as a property in future molecular design, multiple molecular parameters have been investigated.

Firstly, the conductance was considered between the two extreme cases **1 X** = CH_2 and **7 X** = SO_2. An inverse relationship was observed, however when the Seebeck coefficient was plotted against the conductivity (fig S82), there is no observable correlation in the data series.

Similarly, considering theoretically-determined parameters, plotting the Seebeck coefficient versus the electron affinity (fig S83) or the HOMO-LUMO gap (fig S82) resulted in no correlation between these properties. However, plotting the Seebeck coefficient versus the ionization potential (fig S83) showed a trend where increasing ionization potential correlates with increased |S| for five of the compounds in the series. However, given the major deviations from this trend for two compounds(**X** = CH_2 and **X** = NEt) we conclude that ionization potential also does not satisfactorily explain the trend in the Seebeck data.

Considering other experimentally-determined properties, no correlation was found between the Seebeck coefficient and the wavelength of the UV-vis absorption band of the core functionality: this band is an indirect experimental gauge of the HOMO-LUMO gap in the form of the first allowed transition (fig S84). The final experimental parameter that we have used in attempts to find correlation with the Seebeck coefficient is ^{1}H-NMR chemical shift data as a probe for the chemical environment near the site of the bridge **X**. Three different aromatic protons were assessed as probes, i.e. H_a, H_b and H_c (defined in fig S81). However, none of these shows any correlation with the Seebeck data.

Considering the electron-withdrawing or electron-donating effect of the bridge **X**, molecules with either donating (**5**; **X** = NEt) or withdrawing groups (**6** and **7**; X = C=O and SO_2) have the highest |S| values, quickly dismissing this effect as a possible explanation for the trend. It is also clear that aromaticity of the core cannot adequately describe the observed trends in |S| values, as distinctly non-aromatic compounds **1** and **7** (**X** = CH_2 and SO_2) and the most aromatic **2** and **5** (**X** = S and NEt) are at opposite end of the range of |S|. Thus, our best explanation for the trend in the Seebeck data is the one explained in the main paper that focuses on a vibrational parameter and how heat through vibration changes the molecules' structure by perturbing the geometry (main paper).
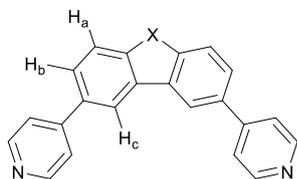

Fig. S81 General structural motif of molecules **1-7** indication the three proton environments (H_a, H_b and H_c) use as probes for correlation study with Seebeck coefficient.
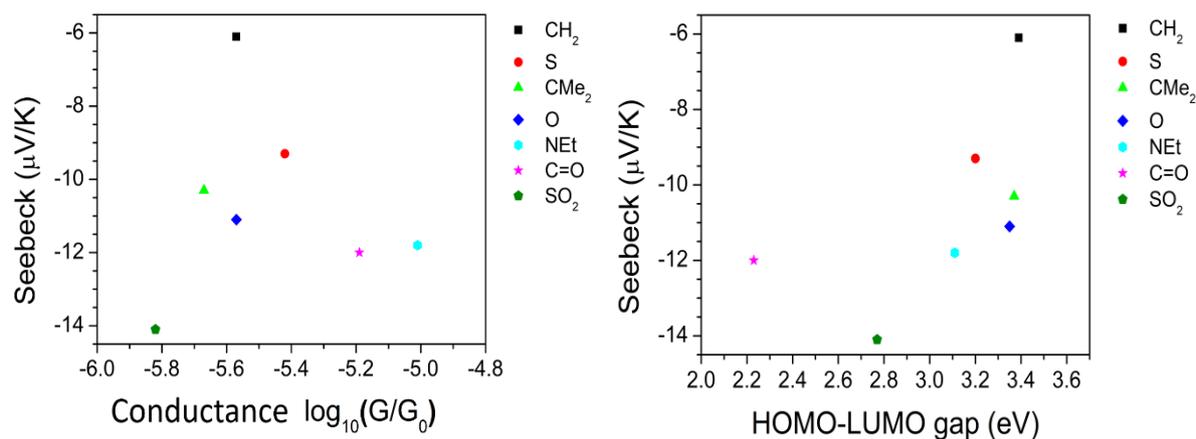
Fig. S82 Correlation plot between measured conductance and measured Seebeck coefficient (left panel) and between theoretical HOMO-LUMO gap and measured Seebeck coefficient (right panel), for the *meta*-connected compounds **1**-**7** (**1** ■black square, **2** ●red circle, **3** ▲light green triangle, **4** ◆blue diamond, **5** ⬡turquoise hexagon, **6** ★magenta star, **7** ⬠ Olive green pentagon).
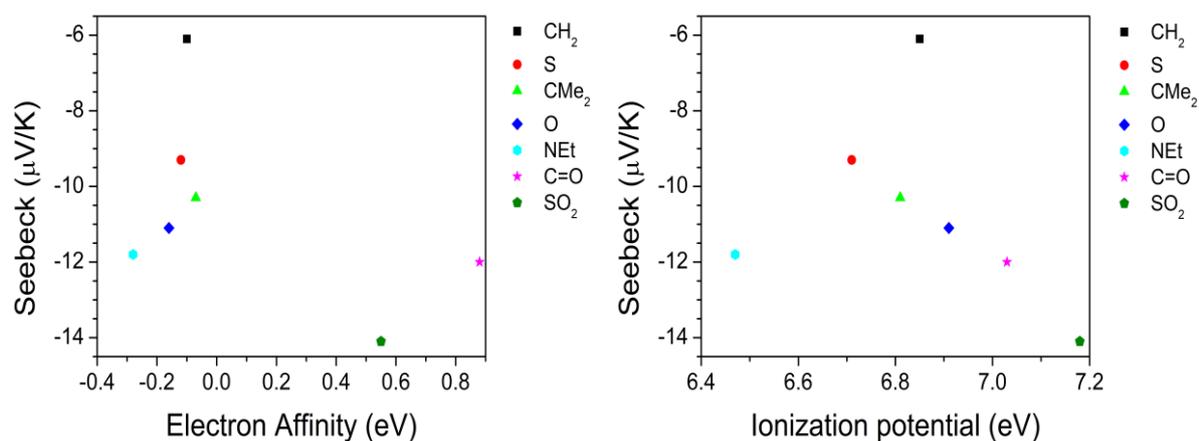
Fig. S83 Correlation plot between theoretical electron affinity and measured Seebeck coefficient (left panel) and Correlation plot between theoretical ionization potential and measured Seebeck coefficient (right panel) for the *meta*-connected compounds **1**-**7** (**1** ■black square, **2** ●red circle, **3** ▲light green triangle, **4** ◆blue diamond, **5** ⬡turquoise hexagon, **6** ★magenta star, **7** ⬠ Olive green pentagon).
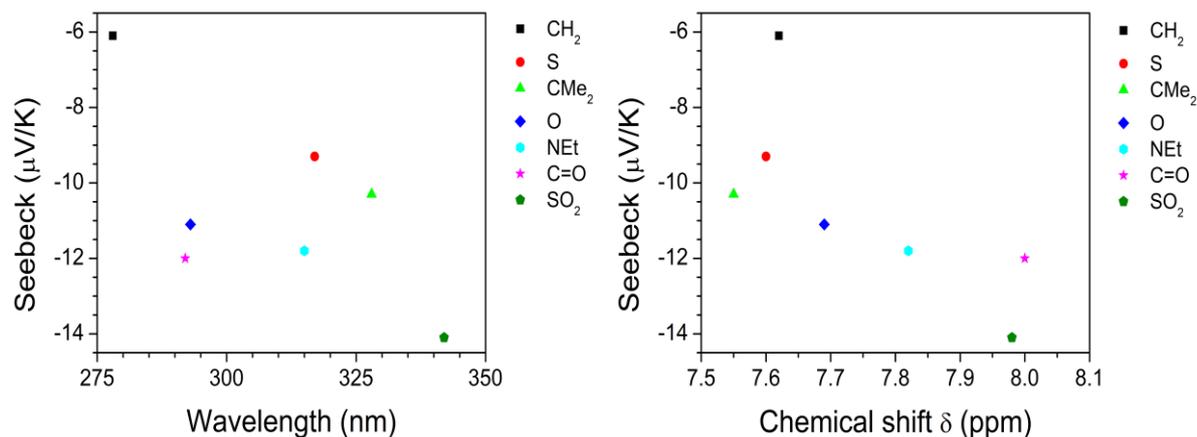
Fig. S84 Correlation plot between measured first UV-vis absorption band (λ$_{max}$ core) and measured Seebeck coefficient (left panel) and Correlation plot between measured 1H-NMR chemical shift of probe H$_a$ (defined in Figure S81) and measured Seebeck coefficient (right panel) for the *meta*-connected compounds **1**-**7** (**1** ■black square, **2** ●red circle, **3** ▲light green triangle, **4** ◆blue diamond, **5** ⬡turquoise hexagon, **6** ★magenta star, **7** ⬟ Olive green pentagon).
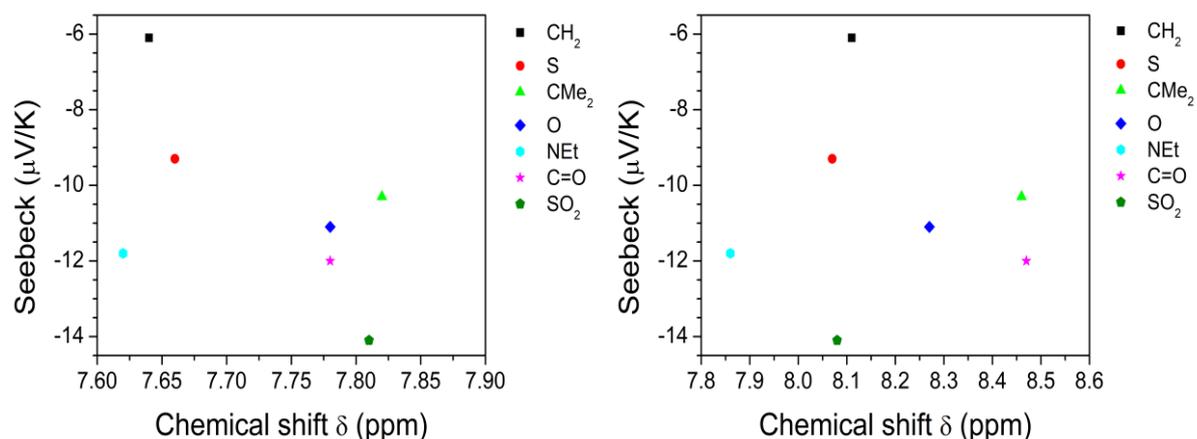
Fig. S85 Correlation plot between measured 1H-NMR chemical shift of probe H$_b$ (defined in Figure S81) and measured Seebeck coefficient (left panel) and Correlation plot between measured 1H-NMR chemical shift of probe H$_c$ (defined in Figure S81) and measured Seebeck coefficient (right panel) for the *meta*-connected compounds **1**-**7** (**1** ■black square, **2** ●red circle, **3** ▲light green triangle, **4** ◆blue diamond, **5** ⬡turquoise hexagon, **6** ★magenta star, **7** ⬟ Olive green pentagon).

S7. References

1. J. P. Perdew, K. Burke and M. Ernzerhof, *Physical Review Letters*, 1996, **77**, 3865-3868.
2. J. M. Soler, E. Artacho, J. D. Gale, A. García, J. Junquera, P. Ordejón and D. Sánchez-Portal, *Journal of Physics: Condensed Matter*, 2002, **14**, 2745-2779.
3. J. Ferrer, C. J. Lambert, V. M. García-Suárez, D. Z. Manrique, D. Visontai, L. Oroszlany, R. Rodríguez-Ferradás, I. Grace, S. W. D. Bailey, K. Gillemot, H. Sadeghi and L. A. Algharagholy, *New Journal of Physics*, 2014, **16**, 093029.
4. A. Alanazy, E. Leary, T. Kobatake, S. Sangtarash, M. T. González, H.-W. Jiang, G. R. Bollinger, N. Agräit, H. Sadeghi, I. Grace, S. J. Higgins, H. L. Anderson, R. J. Nichols and C. J. Lambert, *Nanoscale*, 2019, **11**, 13720-13724.
5. A. Castellan and J. Michl, *Journal of the American Chemical Society*, 1978, **100**, 6824-6827.
6. G. Yzambart, L. Rincón-García, A. A. Al-Jobory, A. K. Ismael, G. Rubio-Bollinger, C. J. Lambert, N. Agraït and M. R. Bryce, *The Journal of Physical Chemistry C*, 2018, **122**, 27198-27204.
7. C. Evangeli, K. Gillemot, E. Leary, M. T. González, G. Rubio-Bollinger, C. J. Lambert and N. Agraït, *Nano Letters*, 2013, **13**, 2141-2145.